







# Control Design of Series-Connected PV-Powered Grid-Forming Converters via Singular Perturbation

Rahul Mallik , *Student Member, IEEE*, Branko Majmunović , *Member, IEEE*,  
Soham Dutta , *Student Member, IEEE*, Gab-Su Seo , *Senior Member, IEEE*, Dragan Maksimović , *Fellow, IEEE*,  
and Brian Johnson , *Member, IEEE*

**Abstract**—Modular architectures that consist of several series-connected dc–ac converters have been a focal point of recent innovations in transformerless medium-voltage applications. In this article, we consider an architecture consisting of dc–ac modules containing a quadruple active bridge dc–dc converter, which generates three floating dc links that feed grid-side dc–ac inverters. Practical implementation of such a converter module in photovoltaic systems requires a variety of controllers that collectively achieve maximum power point tracking, dc-link regulation, and ac-side power control. Design of such multiloop systems is generally quite challenging due to the potential for destabilizing interactions among loops. Here, we propose a design approach where singular perturbation theory is used to decompose the timescales at which each control loop operates and provides a systematic framework for parametric selection. Our approach also ensures system stability of multiple modules with identical controls connected in series across a grid. This article concludes with experimental results of three 1000-W series-connected converter modules across a stiff grid.

**Index Terms**—Cascaded converters, control design, grid-forming, modular inverters, singular perturbation, stability.

## I. INTRODUCTION

RECENT advances in medium-voltage power electronics have pushed renewable energy applications toward transformerless configurations. In this setting, cascaded power

stages are commonly used to distribute voltage stress across multiple circuits. However, the presence of many series-connected converters compounds the difficulties associated with control design. In this article, we focus on photovoltaic (PV) applications where modular converters have a PV string on the dc input and the ac sides of all converters are series-connected across a medium-voltage system. Each converter module features its own dedicated controls to perform maximum power point tracking (MPPT), dc-link regulation, and ac-side grid-forming controls. The primary focus of the ensuing analysis is to propose a systematic framework to design the multiple control loops that exist within each converter. Our approach leverages singular perturbation theory to uncover the distinct timescales that each subsystem operates at and provides a design methodology that is broadly applicable to modular converter structures for medium-voltage settings.

As modular power electronics find greater interest, there is an accompanying evolution from centralized control architectures to distributed and ultimately toward fully decentralized. Focusing on cascaded topologies, such as modular multilevel converters [1] and cascaded H-bridges [2], [3], centralized controllers have been traditionally used to regulate voltages, power, and frequency across the system. As module counts increase, wiring between the growing number of power stages and centralized controller will eventually become untenable. Centralized controllers also suffer from a higher computational burden and introduce a single point-of-failure. Decentralized controllers [4], [5], [6], [7], [8], [9], [10], [11], [12], [13], [14], [15], [16], [17], [18] overcome these difficulties by using module-level control laws that achieve system-level objectives through their inherent electrical coupling. However, decentralization with homogeneous [4], [5], [6], [7], [8], [9], [10], [11], [12], [13], [14], [15] and heterogeneous [16], [17], [18] controllers has focused solely on ac-side synchronization and power sharing. Heterogeneous controllers [16], [17], [18] commonly use a centralized phase-locked-loop (PLL). Homogeneous controllers for cascaded converters have been applied in systems with passive loads [6], [10]. Grid-connected cascaded architectures in [4], [5], [7], [11], [12], and [13] mainly focus on equal power sharing across all modules. Although unequal power sharing is shown experimentally in [9], [14], and [15], analytical stability guarantees are lacking [19]. Moreover, existing works [4], [5], [6], [7], [8], [9], [10], [11], [12], [13], [14], [15], [16], [17], [18] focus exclusively on the series-connected ac-side converter stack

Manuscript received 18 April 2022; revised 10 August 2022; accepted 28 October 2022. Date of publication 10 November 2022; date of current version 14 February 2023. This work was supported by the U.S. Department of Energy Office, Energy Efficiency and Renewable Energy Solar Energy Technologies Office, under Grant DE-EE0008346. This work was authored in part by Alliance for Sustainable Energy, LLC, the manager and operator of the National Renewable Energy Laboratory for the U.S. Department of Energy (DOE) under Contract DE-AC36-08GO28308. The work of Brian Johnson was supported by National Science Foundation CAREER under Award 2143222. Recommended for publication by Associate Editor F. Khan. (*Corresponding author: Rahul Mallik.*)

Rahul Mallik, Soham Dutta, and Brian Johnson are with the Chandra Department of Electrical and Computer Engineering, Cockrell School of Engineering, University of Texas, Austin, TX 78712 USA (e-mail: rmallik@utexas.edu; sdutta@utexas.edu; b.johnson@utexas.edu).

Branko Majmunović is with Kilby Labs, Texas Instruments, Dallas, TX USA (e-mail: b-majmunovic@ti.com).

Gab-Su Seo is with the Power Systems Engineering Center, National Renewable Energy Laboratory, Golden, CO 80401 USA (e-mail: gabsuseo@gmail.com).

Dragan Maksimović is with the Department of Electrical and Computer Engineering, University of Colorado at Boulder, Boulder, CO 80309-0425 USA (e-mail: maksimov@colorado.edu).

Color versions of one or more figures in this article are available at <https://doi.org/10.1109/TPEL.2022.3221331>.

Digital Object Identifier 10.1109/TPEL.2022.3221331

dynamics and lack comprehensive solutions that merge ac- and dc-side control functions under a unified framework. Toward that end, we propose, analyze, and design a cascaded converter system where each module has a multistage dc front-end that entails multiple control loops that are fully integrated with ac-side functions. We also derive analytical stability conditions for unequal power sharing in grid-connected cascaded converters.

Multistage converters are typically controlled with multiple control loops in a nested structure. Multiloop controller design is conventionally tackled by deliberately decomposing the system into faster inner and slower outer control loops. This design principle is applicable to dc–dc converters [20] and dc–ac converters [21], [22], [23], and extends further into system-level secondary and tertiary controllers for system-wide regulation [24]. Note that prior works are predominantly focused on dynamics within a single converter, whereas secondary controllers generally act on slowly varying aggregate models that lack converter-level dynamics. Accordingly, such approaches are insufficient for use in cascaded converter systems with tight coupling at fast timescales.

To address these issues and yield an approach suitable to series-connected modules with upstream power stages, we use singular perturbation methods to systematically identify timescales and formulate a comprehensive controller design. In particular, the converter system is broken up into subsystems whose dynamical equations are transformed into coordinates that automatically induce a timescale separation with fast and slow dynamics [25], [26]. In the proposed architecture, fast dynamics within a particular subsystem are used to generate the reference signal, which is subsequently fed to the next fastest subsystem. This yields a systematic approach for stitching together a chain of dynamical subsystems that form the overall system. Our approach guarantees stability by ensuring that the reference generated by a given subsystem is slower than the fastest timescale of the receiving subsystem in the chain [27, Section 11.3]. With regards to our application, this ensures that MPPT, dc-link regulation, and ac-side functions are systematically partitioned and do not conflict. This is unlike classical approaches that typically neglect the fast dynamics of the upstream reference-generating subsystem in a multiloop structure. On that note, our approach incorporates a richer set of dynamics and offers design guidelines that guarantee stability, which generally do not appear in classical approaches.

Singular perturbation analysis is applied in [28] and [29] to model a grid-following inverter with its inner voltage and current loops, PLL, and filter dynamics. Similar work for grid-forming inverters [28], [30], [31], synchronous machine-dominated power systems [32], [33], and dc–dc converters [34] has also been reported. High-fidelity reduced-order models [28], [34], [35] and analytical stability conditions [22], [29], [30], [36] for single-stage inverter-based parallel-connected inverters have been the main focus of prior literature. In contrast, our work focuses on series-connected ac systems where we study multistage converters comprising nested multiloop controls. The only existing work that uses singular perturbation in the context of series-connected systems [19] focuses on single-stage cascaded converters across a passive load. In contrast, we analyze the grid-connected operation of multistage PV-powered converters.

Despite the fact that the framework in this article is applicable to any system topology composed of several identical multistage converters with ac-side series connections, we focus on the particular setup in Fig. 1. This circuit configuration interfaces a multitude of low-voltage PV strings to a medium-voltage grid [37]. In such a system, the power produced by each PV string is processed by active-bridge converters and pumped into the ac-side interconnection through an inverter. As evident in Fig. 1, this system entails a collection of control loops that must be carefully designed. The main contributions of this article are the following.

- 1) We establish a control design framework that rigorously ensures the stability of complex multistage converter systems with nested and coupled control loops.
- 2) A systematic procedure is put forward where each stage and its controls are decomposed into slow and fast timescales, and the fast modes reveal additional design insights compared to established methods that rely on basic reduced-order models.
- 3) A novel modeling approach translates the nonlinear PV voltage–current curve and input dc-link dynamics into the singular perturbation design framework.
- 4) Experimental results on a prototype consisting of three modules validate decentralized homogeneous controllers for multistage converters with PV generation and series connections on the ac grid side.

This article is structured as follows. Section II provides theoretical background material. Next, Section III describes the dynamics associated with the physical circuitry and control loops within each converter. Control design is covered in Section IV, and we conclude with experimental results in Section V. Section VI concludes this article.

## II. THEORETICAL BACKGROUND

In this section, we present the necessary theoretical and mathematical background that will be harnessed in later sections.

### A. Singular Perturbation Approach

Consider the nonlinear dynamical system

$$\dot{y} = f(y), \quad y \in \mathbb{R}^{n+m}. \quad (1)$$

Assume the preceding system can be decomposed [38] into the two dynamic expressions

$$\dot{x} = f(x, z, \epsilon), \quad x(t_0) = x_0, \quad x \in \mathbb{R}^n, \quad (2)$$

$$\epsilon \dot{z} = g(x, z, \epsilon), \quad z(t_0) = z_0, \quad z \in \mathbb{R}^m, \quad (3)$$

where  $\epsilon \ll 1$  is known as the perturbation parameter. Since  $\epsilon$  is small, (3) captures fast dynamics. Using the approximation  $\epsilon = 0$  yields  $0 = g(x, z, 0)$ , which can be solved to obtain  $z = h(x)$ . We substitute this into (2) to obtain the reduced-order system  $\dot{x} = f(x, h(x), 0)$  with  $n$  states whose solution, denoted as  $\bar{x}$ , captures slow system states. We will refer to this model interchangeably as either the reduced-order or slow-mode model.  $\bar{x}$  closely approximates the actual solution  $x$  such that  $x - \bar{x} = \mathcal{O}(\epsilon)$ .

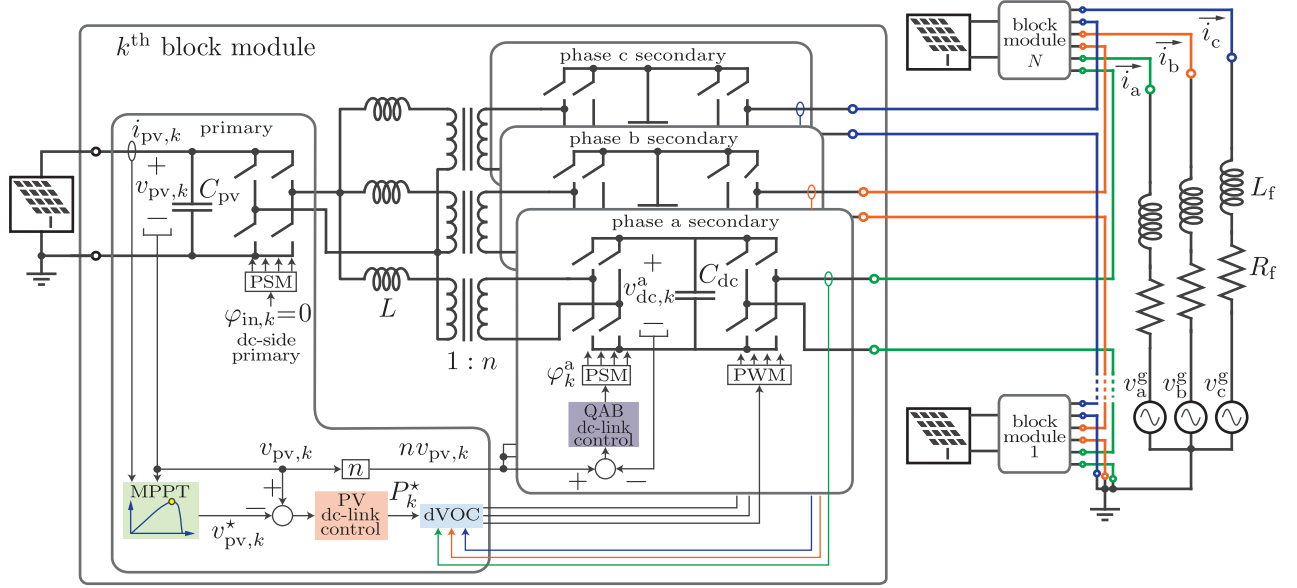


Fig. 1. Multiple converter modules are connected in series across the grid. Each converter module contains three isolated active bridges that each has an output single-phase inverter that transfers power to an ac grid. The various control loops within each converter block are illustrated. This system facilitates efficient power delivery directly into a medium voltage grid.

To gain deeper insights, we now characterize the error between the actual solution  $z(t)$  and its approximation  $\bar{z}(t) = h(\bar{x}(t))$ . Unlike the slow variable,  $x$ , the fast variable  $z$  does not have error bounded by  $\mathcal{O}(\epsilon)$ . In particular,  $z - \bar{z}$  is equal to  $\tilde{z} + \mathcal{O}(\epsilon)$ , where  $\tilde{z}$  evolves as

$$\frac{\partial \tilde{z}}{\partial \tau} = g(x(t_0), \bar{z}(t_0) + \tilde{z}(\tau), 0), \quad (4)$$

where  $\tau = t/\epsilon$  is the fast timescale and intuitively  $\tilde{z}$  captures the error in excess of  $\mathcal{O}(\epsilon)$ . To ensure the original model in (1) as well as the reduced system  $\dot{x} = f(x, h(x), 0)$  are stable, it is necessary to first ensure the fast dynamics in  $\tilde{z}$  are also stable. The conditions [38, Th. 3.1] for stable dynamics in (4) are as follows.

- 1) The equilibrium  $\tilde{z} = 0$  of (4) is asymptotically stable for any initial condition and  $z(t_0) - \bar{z}(t_0)$  belongs to its domain of attraction.
- 2) The eigenvalues of  $\partial g / \partial z$  evaluated for  $\epsilon = 0$  along  $\bar{x}$  and  $\bar{z}$  should have sufficiently negative real parts.

In the ensuing analysis, we will show that these conditions reveal additional guidelines that facilitate the design of nested multiloop systems.

### B. Reference Frame Transformations

Consider the balanced three-phase time-domain signals

$$\begin{aligned} x_a(t) &= X \cos(\theta), \\ x_b(t) &= X \cos\left(\theta - \frac{2\pi}{3}\right), \\ x_c(t) &= X \cos\left(\theta - \frac{4\pi}{3}\right), \end{aligned}$$

where  $X$ ,  $\theta$ , and  $\omega$  denote the amplitude, instantaneous angle, and angular frequency of the time-domain phasor  $x(t) = X e^{j\theta(t)}$ , respectively. These waveforms can be projected onto a rotating pair of orthogonal  $d$  and  $q$  axes using Park's transformation as follows:

$$\begin{bmatrix} x_d \\ x_q \end{bmatrix} = \frac{2}{3} \underbrace{\begin{bmatrix} \cos \theta' & \cos(\theta' - \frac{2\pi}{3}) & \cos(\theta' - \frac{4\pi}{3}) \\ -\sin \theta' & -\sin(\theta' - \frac{2\pi}{3}) & -\sin(\theta' - \frac{4\pi}{3}) \end{bmatrix}}_{\Gamma(\theta'(t))} \begin{bmatrix} x_a \\ x_b \\ x_c \end{bmatrix},$$

where  $\theta'(t) = \int_0^t \omega d\sigma$  defines the instantaneous angle of the frame rotating with frequency  $\omega$ . The components of  $x(t)$  projected onto the axes are denoted as  $x_d$  and  $x_q$ . In the special case  $\theta'(t) = \theta(t)$ , we obtain  $x_d = X$ ,  $x_q = 0$ . All angles are initialized to zero.

### III. SYSTEM MODELING

As illustrated in Fig. 1, the overall system is composed of  $N$  series-connected blocks that have an identical internal structure and are equally rated for apparent power  $S_{\text{rated}}$ . Given the modular structure of the system, we will delineate the detailed structure of the  $k$ -th converter within the stack. As shown, each module has a PV-powered dc input with capacitance  $C_{pv}$  that subsequently feeds a set of three dual active bridge (DAB) converters with a common primary-side bridge. The primary-bridge output connects to three parallel inductances  $L$  that then feed into the respective transformer primary input. Since there are four active bridges within this portion of the system, we refer to this conglomeration as a quadruple active bridge (QAB) converter. Each of the three QAB outputs yields a floating dc

link with capacitance  $C_{dc}$  that connects to a dc–ac inverter for grid integration. The three floating dc links and their respective inverters accommodate power transfer into a three-phase grid. The main purpose of the QAB is to provide isolation between the PV input and the floating ac terminals such that ac-side series interconnections are facilitated.

The QAB converter, which lies at the center of each converter module, acts as the intermediary between the PV input and three-phase ac outputs. From a controls perspective, we will design the closed-loop QAB system to ensure that each DAB behaves as a dc transformer (DCX), where the three floating dc links track the input voltage after scaling by turns ratio  $n$ . Eventually, we will show how the three DCXs, which comprise the QAB, are designed with sufficiently high tracking bandwidth such that the QAB structure is dynamically transparent to the PV- and ac-side controls. Once DCX operation is ensured, the rest of the system closely mirrors a conventional three-phase solar inverter. In particular, for the  $k$ -th module, the PV-side implements an MPPT whose commanded PV voltage  $v_{pv,k}^*$  is realized by modulating the commanded ac power. As shown in Fig. 1, the ac-side power reference emanates from the PV dc-link regulator and the set of three inverter H-bridges is controlled by dispatchable Virtual Oscillator Control (dVOC). From the viewpoint at the module level, the closed-loop dVOC [22] modulates the ac terminals to behave as a controllable ac-side power source. The dVOC dynamics across the stack serve the additional purpose of giving communication-free grid synchronization and power (i.e., voltage) sharing. Having said that, the proposed design approach is equally applicable to any other grid-forming technique, such as conventional droop [39] or virtual synchronous machines [40].

#### A. QAB With Floating DC Links

The primary-side bridge is common to each of the three floating secondary bridges. All four bridges are modulated to produce an ac voltage waveform with 50% duty ratio, and the primary-side bridge acts as an angular reference to the remaining three others. Accordingly, the phase shifts of the secondary bridge waveforms relative to the primary side will act as our control signal for dc-link voltage regulation. In particular, we denote the phase shift of the secondary DAB bridge associated with the  $j$ -th ac phase within the  $k$ -th module as  $\varphi_k^j$ , where  $j \in \{a, b, c\}$ . The voltage across each of the floating dc links evolves as [41]

$$C_{dc} \frac{dv_{dc,k}^j}{dt} = \frac{v_{pv,k}}{nL\omega_{sw}} \varphi_k^j \left(1 - \frac{\varphi_k^j}{\pi}\right) - \frac{P_k^j}{v_{dc,k}^j}, \quad (5)$$

where  $\omega_{sw}$  is the DAB switching frequency in rad/s,  $\varphi_k^j$  is the phase shift of each secondary bridge with respect to the primary, and  $v_{pv,k}$  is the dc voltage across the PV input.  $P_k^j$  denotes the power transferred from the primary to the  $j$ -th secondary.

A proportional–integral (PI) controller ensures DCX operation such that the dc voltage across  $C_{dc}$  tracks  $nv_{pv}$ . This gives the following control law:

$$\dot{\varphi}_k^j = k_{p,dc} (nv_{pv,k} - v_{dc,k}^j) + C_{dc} k_{i,dc} \int (nv_{pv,k} - v_{dc,k}^j) dt \quad (6)$$

This controller is replicated across the three dc links, where  $j \in \{a, b, c\}$ . The proportional and integral gains are denoted as  $k_{p,dc}$  and  $k_{i,dc}$ , respectively.

The power  $P_k^j$  extracted from each dc link and transferred to its corresponding ac terminals takes the form of a nonlinear time-varying double-frequency pulsating waveform. Assuming sinusoidal steady-state conditions on the ac side, each power contribution in (5) is

$$\begin{aligned} P_k^a &= V_k \cos(\theta_k) I \cos(\theta_i), \\ P_k^b &= V_k \cos\left(\theta_k - \frac{2\pi}{3}\right) I \cos\left(\theta_i - \frac{2\pi}{3}\right), \\ P_k^c &= V_k \cos\left(\theta_k + \frac{2\pi}{3}\right) I \cos\left(\theta_i + \frac{2\pi}{3}\right), \end{aligned}$$

where  $I$  and  $V_k$  are the peak ac current and output voltage at the ac terminals of the  $k$ -th converter, respectively, and  $\theta_i$  is the phase angle between the current and global reference frames. The controls that dictate ac-side waveforms will be described in the next section.

To obtain a model that does not contain time-varying nonlinearities, we sum the dynamical equations in (5) for all the three phases to obtain the following lumped model:

$$\sum_j C_{dc} \frac{dv_{dc,k}^j}{dt} = \sum_j \frac{v_{pv,k}}{nL\omega_{sw}} \varphi_k^j \left(1 - \frac{\varphi_k^j}{\pi}\right) - \sum_j \frac{P_k^j}{v_{dc,k}^j}$$

Total module-level ac-side power, denoted as  $P_k$ , under balanced operation is

$$P_k = \sum_j P_k^j = P_k^a + P_k^b + P_k^c = \frac{3}{2} V_k i_d, \quad (7)$$

where  $i_d$  is the first component of  $i_{dq} = [i_d, i_q]^\top = \Gamma_{dq}(\delta_k) i$  and  $i = [i_a, i_b, i_c]^\top$  is a vector of the three-phase currents. In subsequent analysis, we will show that the relative frame angle of the  $k$ -th module  $\delta_k$  is generated by its ac-side controller.

Within a given module, we assume that the floating dc-link voltage for each phase  $v_{dc,k}^j$  is approximately equal to its steady-state value  $v_{dc,k}^0$ . This approximation can further be substantiated using the linearization methods in [42]. Furthermore, each DAB is assumed to operate with small phase shifts such that  $(\varphi_k^j)^2$  is negligibly small [43]. Taken together, these modeling constructs allow us to convert the dynamics in (5) into the simplified model given by

$$C_{dc} \frac{dv_{dc,k}^j}{dt} = \frac{v_{pv,k}}{nL\omega_{sw}} \varphi_k^j - \frac{P_k^j}{v_{dc,k}^0}.$$

Furthermore, since  $P_k$  does not depend on time [see (7)], we can simplify the lumped model as

$$C_{dc} \frac{dv_{dc,k}}{dt} = \frac{v_{pv,k}}{nL\omega_{sw}} \varphi_k - \frac{P_k}{3v_{dc,k}^0}, \quad (8)$$

where lumped variables  $v_{dc,k}$  and  $\varphi_k$  are defined as

$$v_{dc,k} = \frac{1}{3} \sum_j v_{dc,k}^j, \quad \varphi_k = \frac{1}{3} \sum_j \varphi_k^j.$$



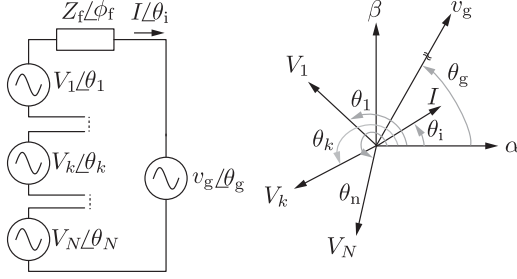


Fig. 2. AC-side phasor model of  $N$  series-connected modules across the grid and an output filter. The amplitude and angle of each set of ac terminals is modulated by an independent dVOC loop.

### B. AC-Side Dynamics

The three-phase grid voltages take the form

$$\begin{bmatrix} v_g^a \\ v_g^b \\ v_g^c \end{bmatrix} = \begin{bmatrix} V_g \cos(\theta_g) \\ V_g \cos(\theta_g - \frac{2\pi}{3}) \\ V_g \cos(\theta_g - \frac{4\pi}{3}) \end{bmatrix}, \quad (9)$$

where  $V_g$  is the nominal peak grid voltage and  $\theta_g = \int_0^t \omega_g d\sigma$  is the instantaneous grid angle. We assume the grid provides a stiff voltage across an output  $RL$  filter and  $N$  series-connected modules.

Each set of module-level three-phase H-bridges is modulated with the dVOC [22], [44] dynamics given by

$$\dot{V}_k = \mu V_k \left( \left( \frac{V_g}{N} \right)^2 - V_k^2 \right) - \frac{2\eta}{3V_k} (Q_k - Q_k^*), \quad (10)$$

$$\dot{\theta}_k = \omega_k = \omega_0 - \frac{2\eta}{3V_k^2} (P_k - P_k^*), \quad (11)$$

where  $\mu$  and  $\eta$  are control gains, and  $\omega_0$  is the nominal grid frequency. The peak voltage generated by each single phase inverter is denoted as  $V_k$ , and the three-phase waveforms are in the vector  $v_k = [v_k^a, v_k^b, v_k^c]^T$ . Active and reactive powers delivered by the  $k$ -th module are represented as  $P_k$  and  $Q_k$ , respectively. Similarly,  $P_k^*$  and  $Q_k^*$  denote the corresponding references for active and reactive powers, respectively. In subsequent analysis, we will show that  $P_k^*$  is generated by an upstream control loop, whereas  $Q_k^*$  will be assumed constant. The characteristic nonlinear droop offered by dVOC ensures a coupling between active power and frequency, which, in turn, gives decentralized power sharing and synchronization. The ac-side phasor model is summarized in Fig. 2, where  $Z_f = \sqrt{R_f^2 + (L_f\omega_0)^2}$  and  $\phi_f = \tan^{-1}(L_f\omega_0/R_f)$  capture the line impedance amplitude and its angle, respectively.

Setting the derivatives in (10)–(11) to zero, we evaluate the largest deviations in steady-state voltage and frequency as  $P_k$  and  $Q_k$  reach their maximal value of  $S_{\text{rated}}$ . The largest deviation in steady-state voltage and frequency around the nominal values of  $V_g/N$  and  $\omega_0$ , respectively, are denoted as  $\Delta V$  and  $\Delta\omega$ , respectively. It can be shown [44] that the oscillator gains are related to the voltage and frequency tradeoffs as follows:

$$\eta \leq \frac{3 \Delta\omega \left( \frac{V_g}{N} - \Delta V \right)^2}{2 S_{\text{rated}}}, \quad (12)$$

$$\mu \geq \frac{\Delta\omega}{\Delta V \left( 2 \frac{V_g}{N} - \Delta V \right)} \quad (13)$$

To facilitate analysis, we define angles and their derivatives with respect to the grid voltage angle  $\theta_g$  such that

$$\dot{\delta}_k = \dot{\theta}_k - \dot{\theta}_g = \omega_k - \omega_g,$$

where  $\delta_k$  captures the  $k$ -th relative angle difference. Without loss of generality, we assume that the grid frequency is fixed at the nominal value such that  $\omega_g = \omega_0$ , and the angular dynamics reduces to

$$\dot{\delta}_k = -\frac{2\eta}{3V_k^2} (P_k - P_k^*). \quad (14)$$

$N$  series-connected sets of ac terminals with the aforementioned control give the following line filter dynamics:

$$\begin{aligned} \sum_{k=1}^N V_k \cos \delta_k &= L_f \frac{di_d}{dt} - L_f \omega i_q + R_f i_d + V_g, \\ \sum_{k=1}^N V_k \sin \delta_k &= L_f \frac{di_q}{dt} + L_f \omega i_d + R_f i_q \end{aligned} \quad (15)$$

### C. PV Terminal Dynamics

Energy buffering between the PV panel and QAB stage is provided by the PV-side capacitance  $C_{pv}$ . The PV voltage dynamics can be expressed as

$$\frac{d}{dt} \left( \frac{1}{2} C_{pv} v_{pv,k}^2 \right) = P_{in,k} - P_{out,k}, \quad (16)$$

where  $P_{in,k}$  is the PV-generated power and  $P_{out,k}$  is power delivered to the QAB. Assuming the QAB circuitry is lossless, it follows that  $P_{out,k}$  equals the ac-side power  $P_k$  for the  $k$ -th module. The input power is expressed as  $P_{in,k} = v_{pv,k} i_{pv,k}$ , where the PV current  $i_{pv,k}$  takes the form

$$i_{pv,k} = i_{o,k} - i_{sat,k} \left( e^{\frac{v_{pv,k} + i_{pv,k} R_{s,k}}{a V_T}} - 1 \right). \quad (17)$$

This is known as the single-diode model [45], where for the  $k$ -th module  $i_{o,k}$  is the photocurrent,  $i_{sat,k}$  is the diode saturation current,  $R_{s,k}$  is the series resistance,  $V_T$  is the thermal voltage, and  $a$  is the diode ideality constant.

Next, we denote the small-signal resistance of the PV modules as  $r_{pv,k}$  and define it [46] as

$$r_{pv,k} = -\frac{\partial v_{pv,k}}{\partial i_{pv,k}} = \frac{-a V_T - i_{sat,k} R_{s,k} e^{\frac{v_{pv,k} + i_{pv,k} R_{s,k}}{a V_T}}}{i_{sat,k} e^{\frac{v_{pv,k} + i_{pv,k} R_{s,k}}{a V_T}}}.$$

A small-signal dynamic model is obtained by the addition of perturbations to  $v_{pv,k}$ ,  $P_{in,k}$ , and  $P_{out,k}$  in (16). This gives

$$\begin{aligned} \frac{d}{dt} \left( \frac{1}{2} C_{pv} (V_{pv,k} + \tilde{v}_{pv,k})^2 \right) &= (V_{pv,k} + \tilde{v}_{pv,k}) (I_{pv,k} + \tilde{i}_{pv,k}) \\ &\quad - (P_k^* + \tilde{p}_k^*). \end{aligned}$$

To streamline notation, we drop the  $\tilde{\cdot}$  notation for small-signal terms hereafter. We retain first- and second-order terms while

neglecting the dc components to get the approximate plant model

$$V_{pv,k} C_{pv} \frac{dv_{pv,k}}{dt} = f_{pv}(v_{pv,k}, i_{pv,k}, r_{pv,k}) - p_k^*. \quad (18)$$

We will simplify (18) by approximating the value of  $f_{pv,k}(v_{pv,k}, i_{pv,k}, r_{pv,k})$  at distinct regions across the PV curve. Toward that end, from Fig. 4 note that  $r_{pv,k}$  is close to  $V_{mpp,k}/I_{mpp,k}$  near the maximum power point (i.e., when  $V_{mpp,k} - \epsilon/2 < v_{pv,k} < V_{mpp,k} + \epsilon/2$ ) and drops (grows) to small (large) values when approaching the open (short) circuit operating points. After we define  $R_{mpp,k} := V_{mpp,k}/I_{mpp,k}$ , we approximate  $f_{pv,k}(\cdot)$  as taking on the following forms across the aforementioned operating regimes:

$$f_{pv,k}(\cdot) = \begin{cases} I_{pv,k} v_{pv,k}, & \text{when } v_{pv,k} < V_{mpp,k} - \frac{\epsilon}{2} \\ -\frac{v_{pv,k}^2}{R_{mpp,k}}, & \text{when } V_{mpp,k} - \frac{\epsilon}{2} < v_{pv,k} < V_{mpp,k} + \frac{\epsilon}{2} \\ -\frac{V_{pv,k}}{r_{pv,k}} v_{pv,k}, & \text{when } v_{pv,k} > V_{mpp,k} + \frac{\epsilon}{2} \end{cases}$$

The PV dc-link controller ensures that the  $k$ -th PV voltage  $v_{pv,k}$  is regulated to follow the command  $v_{pv,k}^*$ , which is produced by the MPPT. To this end, a PI controller processes the voltage error and generates the ac-side power reference,  $P_k^*$ . The PV dc-link controller is given by

$$P_k^* = k_{p,pv}(v_{pv,k} - v_{pv,k}^*) + C_{pv} k_{i,pv} \int (v_{pv,k} - v_{pv,k}^*) dt. \quad (19)$$

#### D. MPPT Control

To evaluate MPPT performance, we seek a simplified version of (18) and linearize the algebraic expression in (17) around the MPP [47] to obtain

$$i_{pv,k} = I_{mpp,k} - \frac{1}{R_{mpp,k}}(v_{pv,k} - V_{mpp,k}). \quad (20)$$

To track the MPP, we employ the integral control law [47] that acts on the slope of the PV power-voltage curve as follows:

$$v_{pv,k}^* = \gamma \int \frac{\partial(v_{pv,k} i_{pv,k})}{\partial v_{pv,k}} dt \quad (21)$$

Since our main focus is on cascaded converter dynamics with both dc- and ac-side controllers, we use a relatively simple MPPT that only guarantees local peak power tracking. The authors refer to [48] and [49] for techniques that can be used to modify (21) for global peak power tracking.

#### IV. SINGULAR PERTURBATION MODELING AND CONTROL DESIGN

For each of the subsystems described in Section III, we now shift our focus to designing the controllers after application of singular perturbation theory. Our overall strategy is predicated on an intuition of how the various subsystems within each module interact and seek a logical ordering of timescales over

which they operate. Toward this objective, we first apply singular perturbation to each subsystem such that it is partitioned into fast and slow modes. This yields a form that is amenable to design such that we can obtain the preordained ordering and separation of timescales while also guaranteeing stability within and among subsystems. In the ensuing analysis we apply the aforementioned strategy and describe each subsystem sequentially from fastest to slowest.

##### A. QAB DC-Link Voltage Regulation

1) *State Equations*: DC-link voltage control is achieved through the PI regulator in (6). To cast the subsystem in (5)–(6) into the singular perturbation framework, we define two new states as

$$e_{1,k} := nv_{pv,k} - v_{dc,k}, \quad e_{2,k} := C_{dc} \int_0^\tau e_{1,k} d\sigma + e_{2,k}(0),$$

where  $\tau = t/C_{dc}$  is the new time variable associated with the fast mode. Now (5) and (6) can be rewritten as

$$C_{dc} \frac{de_{1,k}}{d\tau} = \frac{-v_{pv,k}}{nL\omega_{sw}}(k_{p,dc}e_{1,k} + k_{i,dc}e_{2,k}) + \frac{P_k}{3v_{dc,k}^0}, \quad (22)$$

$$\frac{de_{2,k}}{d\tau} = C_{dc}e_{1,k}. \quad (23)$$

Drawing a parallel between (3) and (22), we set  $C_{dc}$  to zero, obtain the algebraic solution of  $\bar{e}_{1,k}$ , and substitute that into (23) to obtain the reduced-order model as follows:

$$\frac{d\bar{e}_{2,k}}{dt} = -\frac{k_{i,dc}}{k_{p,dc}}\bar{e}_{2,k} + \left(\frac{v_{pv,k}}{nL\omega_{sw}}\right)^{-1} \frac{P}{3k_{p,dc}v_{dc,k}^0} \quad (24)$$

Mirroring (4), the fast mode model is

$$\frac{d\tilde{e}_{1,k}}{d\tau} = -\frac{v_{pv,k}k_{p,dc}}{nC_{dc}L\omega_{sw}}\tilde{e}_{1,k} =: -\omega_{QAB}^f \tilde{e}_{1,k}, \quad (25)$$

where we recall from (4) that  $\tilde{e}_{1,k}$  captures the error in excess of  $\mathcal{O}(\epsilon)$  in  $e_{1,k} - \bar{e}_{1,k}$ .

2) *Stability and Control Parameter Selection*: Following the stability conditions in Section II-A, it is necessary to ensure  $k_{p,dc} \geq 0$  and  $k_{i,dc} \geq 0$ . From (24), the effective bandwidth of the QAB loop is

$$\omega_{QAB} = \frac{k_{i,dc}}{k_{p,dc}}. \quad (26)$$

This leads us to the first stability criterion as

$$\omega_{QAB} \ll \omega_{QAB}^f \ll \omega_{sw}, \quad (27)$$

where  $\omega_{QAB}$  corresponds to the slower acting integral control and  $\omega_{QAB}^f$  captures the bandwidth of the fast mode model in (25). After appropriate substitutions from (25)–(26) into (27) give the following guideline for control gain selection:

$$\frac{k_{i,dc}}{k_{p,dc}} \ll \frac{v_{pv,k}k_{p,dc}}{nC_{dc}L\omega_{sw}} \ll \omega_{sw}. \quad (28)$$

In addition to (27), stability of the timescale-separated QAB dc-link subsystem in (22)–(23) depends on the value of the

perturbation parameter  $C_{dc}$ . We rigorously derive the upper limit of  $C_{dc}$  in Appendix A. Similar conditions can be computed for each and every subsystem, but we withhold these for the sake of paper compactness.

### B. DVOC-Based Inverter Control

1) *State Equations*: The nonlinear control law given by (10)–(14) exhibits slower dynamics than the plant in (15). This follows from the observation that the small perturbation parameter  $L_f/R_f$  gives fast line dynamics. Hence, we set  $L_f/R_f = 0$  and obtain the following algebraic solution from (15):

$$i_d = \frac{\sum_{k=1}^N V_k \cos(\delta_k - \phi_f) - V_g \cos(\phi_f)}{Z_f}, \quad (29)$$

$$i_q = \frac{\sum_{k=1}^N V_k \sin(\delta_k - \phi_f) + V_g \sin(\phi_f)}{Z_f}, \quad (30)$$

where we recall that  $Z_f$  and  $\phi_f$  denote the line impedance amplitude and angle, respectively. It follows that the  $i$ th module delivers the active and reactive power

$$P_i = \frac{3V_i i_d \cos \delta_i}{2}, \quad Q_i = -\frac{3V_i i_q \sin \delta_i}{2},$$

and substitution of (29)–(30) gives

$$\begin{aligned} P_i &= \sum_{k=1}^N \frac{3V_k V_i}{2Z_f} \cos(\delta_k - \delta_i - \phi_f) - \frac{3V_g V_i}{2Z_f} \cos(-\delta_i - \phi_f), \\ Q_i &= -\sum_{k=1}^N \frac{3V_k V_i}{2Z_f} \sin(\delta_k - \delta_i - \phi_f) + \frac{3V_g V_i}{2Z_f} \sin(-\delta_i - \phi_f). \end{aligned} \quad (31)$$

Insertion of (31) into (14) gives the angle dynamics

$$\begin{aligned} \dot{\delta}_i &= -\frac{2\eta}{3V_i^2} \left( \sum_{k=1}^N \frac{3V_k V_i}{2Z_f} \cos(\delta_k - \delta_i - \phi_f) \right. \\ &\quad \left. - \frac{3V_g V_i}{2Z_f} \cos(-\delta_i - \phi_f) - P_i^* \right). \end{aligned} \quad (32)$$

To obtain a small-signal model for the  $i$ th inverter angle, we linearize (32) as

$$\begin{aligned} \dot{\tilde{\delta}}_i &= \frac{\eta}{V_i Z_f} \left( \sum_{\substack{k=1 \\ k \neq i}}^N V_k \sin(\delta_i - \delta_k + \phi_f) - V_g \sin(\delta_i + \phi_f) \right) \tilde{\delta}_i \\ &\quad - \frac{\eta}{V_i Z_f} \sum_{\substack{k=1 \\ k \neq i}}^N V_k \sin(\delta_i - \delta_k + \phi_f) \tilde{\delta}_k, \end{aligned} \quad (33)$$

where  $\tilde{\delta}_i$  represents a small-signal perturbation in  $\delta_i$ . This is rewritten in matrix to obtain

$$\dot{\tilde{\delta}} = (\eta/Z_f) A \tilde{\delta},$$

where  $\delta = [\delta_1, \delta_2, \dots, \delta_N]^T$  is the state vector and the state matrix  $A$  is

$$A = \begin{bmatrix} \sum_{\substack{k=1 \\ k \neq 1}}^N \xi_{1k} - \xi_1 & -\xi_{12} & \dots & -\xi_{1N} \\ -\xi_{21} & \sum_{\substack{k=1 \\ k \neq 2}}^N \xi_{2k} - \xi_2 & \dots & -\xi_{2N} \\ \vdots & \vdots & \ddots & \vdots \\ -\xi_{N1} & -\xi_{N2} & \dots & \sum_{\substack{k=1 \\ k \neq N}}^N \xi_{Nk} - \xi_N \end{bmatrix}. \quad (34)$$

We define  $\xi_{ik}$  and  $\xi_i$  in (34) as

$$\xi_{ik} := \frac{V_k}{V_i} \sin(\delta_i - \delta_k + \phi_f), \quad \xi_i := \frac{V_g}{V_i} \sin(\delta_i + \phi_f). \quad (35)$$

The Gershgorin discs [50] for  $A$  are defined as

$$\left\{ z \in \mathbb{C} : |z - a_{ii}| \leq \sum_{\substack{j=1 \\ j \neq i}}^N |a_{ij}| \right\}, \quad i = 1, 2, \dots, N.$$

From [50, Th. 6.1.1], we know that every eigenvalue of  $A$  will be located within the union of the above discs denoted as

$$G(A) := \bigcup_{i=1}^N \left\{ z \in \mathbb{C} : |z - a_{ii}| \leq \sum_{\substack{j=1 \\ j \neq i}}^N |a_{ij}| \right\}.$$

If under all operating conditions,  $G(A)$  is shown to lie entirely within the left-half plane (LHP), a sufficient condition of stability for the  $i$ th module, where  $i \in \{1, 2, \dots, N\}$ , is

$$|\lambda_i - a_{ii}| \leq \sum_{\substack{j=1 \\ j \neq i}}^N |a_{ij}| \Rightarrow -\sum_{\substack{j=1 \\ j \neq i}}^N |a_{ij}| \leq \lambda_i - a_{ii} \leq \sum_{\substack{j=1 \\ j \neq i}}^N |a_{ij}|.$$

For all eigenvalues to be in the LHP, we need

$$\lambda_i \leq \sum_{\substack{j=1 \\ k \neq i}}^N |a_{ij}| + a_{ii} \leq 0, \quad i = 1, 2, \dots, N. \quad (36)$$

We substitute the value of  $a_{ij}$ th element of  $A$  from (34) into (36) to obtain the following stability condition:

$$\sum_{\substack{k=1 \\ k \neq i}}^N |\xi_{ik}| + \sum_{\substack{k=1 \\ k \neq i}}^N \xi_{ik} - \xi_1 \leq 0 \quad (37)$$

Using the identity  $\sum_k |x_k| \geq \sum_k x_k$ , a simplified but stricter condition is given by

$$2 \sum_{\substack{k=1 \\ k \neq i}}^N |\xi_{ik}| - \xi_1 \leq 0. \quad (38)$$

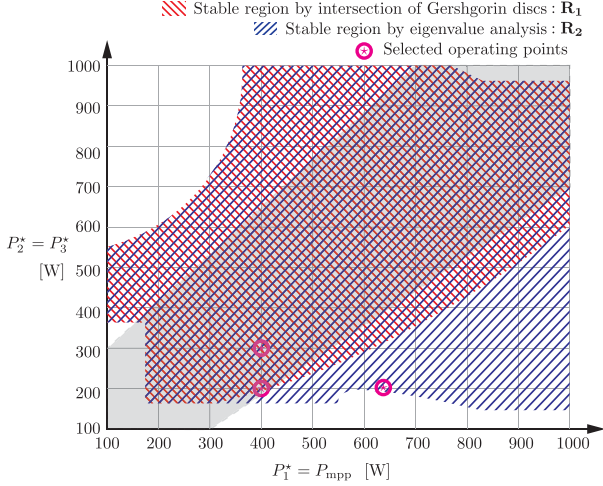


Fig. 3. Example case of  $N = 3$  modules where unit #1 is powered from PV, whereas units #2 and #3 are powered with dc supply.  $\mathbf{R}_1$  and  $\mathbf{R}_2$  indicate regions where stable operation is guaranteed via eigenvalue analysis. The gray area shows 30% power mismatch between  $P_1^*$  and either  $P_2^*$  or  $P_3^*$ .

Assuming equal module voltages such that  $V_j \approx V_k \approx V_g/N$ , we substitute  $\xi_{ij}$  and  $\xi_i$  from (35) into (38) to obtain the following stability criterion:

$$2 \sum_{\substack{k=1 \\ k \neq i}}^N |\sin(\delta_i - \delta_k + \phi_f)| \leq N \sin(\delta_i + \phi_f) \quad (39)$$

The preceding analysis is generalized and does not make any assumptions about equal module voltage or power. We substantiate the preceding analysis with a numerical example which mirrors the experimental setup in Section V.

We choose  $N = 3$ , where module #1 is powered by a PV source and modules #2 and #3 are powered by dc voltage sources and have power commands  $P_2^* = P_3^*$ . In Fig. 3, the unshaded region is infeasible for the system parameters in Table I. The blue hatched region, denoted as  $\mathbf{R}_2$ , represents  $P_i^*, i \in \{1, 2, 3\}$  for which the cascaded system is stable by eigenvalue analysis. Shown in red-hatch,  $\mathbf{R}_1$  represents  $P_i^*, i \in \{1, 2, 3\}$  for which the system is sufficiently stable according to (37). Stability guarantees of the simplified condition in (39) approximately correspond to  $\mathbf{R}_1$ . The gray region where  $i, j \ni |P_i^* - P_j^*| < 0.3P_{\max}$  represents power mismatch between PV panels due to nonuniform insolation, manufacturing tolerances, and temperature differences. These variations yield power differences that are generally well within region  $\mathbf{R}_1$  where stability is guaranteed. Experimental operating points, marked as  $\star$ , are at the margins of theoretical stability. Having demonstrated stable MPPT operation for those points in Section V, we expect stable operation in the gray region in Fig. 3 where mismatches are reasonable and practical.

2) *Stability and Control Parameter Selection:* The dVOC controllers are simultaneously responsible for module-level power tracking and system-level synchronization. Assuming equal reactive power references such that  $Q_i^* = Q_j^*$ ,  $\forall i, j \in \{1, N\}$ , it follows from (10) that all module voltages are equal and  $V_i = V_j \approx V_g/N$ ,  $\forall i, j \in \{1, N\}$ . Furthermore, since the voltage dynamics are significantly faster than the

TABLE I  
SYSTEM PARAMETERS

	Symbol	Description	Value	Units
Ac system	$S_{\text{rated}}$	module VA rating	3000	VA
	$N$	modules in series	3	
	$V_g$	rms line-neutral grid voltage	90	V
	$\omega_{\text{nom}}$	rated frequency	60	Hz
	$L_f$	inductance	2.4	mH
	$R_f$	resistance	4.2	$\Omega$
	$\mu$	dVOC parameter I	1	$V^{-2}s^{-1}$
QAB dc links	$\eta$	dVOC parameter II	100	$\Omega s^{-1}$
	$V_{\text{dc}}^0$	nominal dc voltage	100	V
	$\omega_{\text{sw}}$	switching frequency	100	kHz
	$L$	inductance	26	$\mu\text{H}$
	$n$	turns ratio	0.5	
	$C_{\text{pv}}$	input capacitance	660	$\mu\text{F}$
	$C_{\text{dc}}$	dc-link capacitance	200	$\mu\text{F}$
MPPT & PV	$k_{\text{p,dc}}$	proportional gain	2.05	$\Omega^{-1}$
	$k_{\text{i,dc}}$	integral gain	1290	$(\Omega s)^{-1}$
	$V_{\text{oc}}$	open-circuit voltage	200	V
	$I_{\text{sc}}$	short-circuit current	4.0	A
	$V_{\text{mpp}}$	MPP voltage	160	V
	$I_{\text{mpp}}$	MPP current	3.0	A
	$k_{\text{p,pv}}$	proportional gain	6	A
Bandwidth	$k_{\text{i,pv}}$	integral gain	6.53	$\text{As}^{-1}$
	$\gamma$	MPPT gain	0.01	V/V
	$\omega_{\text{QAB}}^f$	QAB fast mode	10	kHz
	$\omega_{\text{QAB}}$	QAB slow mode	100	Hz
	$\omega_{\text{dVOC}}$	dVOC	8.44	Hz
	$\omega_{\text{cc}}^f$	CCR-PV fast mode	3.06	Hz
	$\omega_{\text{cv}}^f$	CVR-PV fast mode	7.24	Hz
	$\omega_{\text{cc}}$	CCR-PV slow mode	0.26	Hz
	$\omega_{\text{cv}}$	CVR-PV slow mode	0.16	Hz
	$\omega_{\text{mppt}}$	MPPT control	0.09	Hz

angle dynamics (see Appendix B), we can decouple the voltage dynamics from the angle dynamics to simplify (32) as

$$\dot{\delta}_i = -\frac{\eta}{Z_f} \left( \sum_{k=1}^N \cos(\delta_k - \delta_i - \phi_f) - N \cos(-\delta_i - \phi_f) - P_i^* \right). \quad (40)$$

To obtain closed-form expressions for bandwidth that enable us to enforce timescale separation among the various subsystems, we now assume equal power delivery for all modules. Equation (14) indicated that when module angles become identical  $\delta_i = \delta_j$ ,  $\forall i, j \in \{1, N\}$ , the resulting angle dynamics are given by

$$\dot{\delta}_i = -\frac{\eta}{Z_f} (N \cos(\phi_f) - N \cos(\delta_i + \phi_f) - P_i^*). \quad (41)$$

Without loss of generality, assume the line has equal reactance and resistance such that  $\phi_f = \pi/4$  and (41) becomes

$$\dot{\delta}_i = -\frac{\eta N}{Z_f \sqrt{2}} \left( 1 - \cos \delta_i + \sin \delta_i - \frac{P_i^* \sqrt{2}}{N} \right). \quad (42)$$

Under small values of  $\delta_i$  in (42), the effective bandwidth of the system is

$$\omega_{\text{dVOC}} = \frac{\eta N}{Z_f \sqrt{2}}. \quad (43)$$

Stability of (10) necessitates  $\mu, \eta > 0$  since  $V_k$  is positive. Moreover, since we need timescale separation between  $\omega_{\text{dVOC}}$



and  $\omega_{QAB}$ , it follows that (43) and (26) imply

$$\omega_{dVOC} \ll \omega_{QAB} \rightarrow \frac{\eta N}{Z_f \sqrt{2}} \ll \frac{k_{i,dc}}{k_{p,dc}}. \quad (44)$$

Recall the frequency droop in (12) and note that the frequency deviation parameter  $\Delta\omega$  can be adjusted to ensure (44) is met. The desired voltage tradeoff in (13) informs the choice of  $\mu$  and the numerical approach in [5] can be used to further substantiate ac-side stability.

### C. PV DC-Link Control

1) *State Equations:* The PI controller in (19) regulates  $v_{pv,k}$ . To cast (18)–(19) into the singular perturbation framework, we define two new states as

$$e_{1,k} = v_{pv,k} - v_{pv,k}^*, \quad e_{2,k} = C_{pv} \int_0^\tau e_{1,k} d\sigma + e_{2,k}(0),$$

where  $\tau = t/C_{pv}$  is the new time variable for the fast mode. Now (18)–(19) can be rewritten as

$$C_{pv} \frac{de_{1,k}}{d\tau} = \begin{cases} \frac{I_{pv,k} - k_{p,pv}}{V_{pv,k}} e_{1,k} - \frac{k_{i,pv}}{V_{pv,k}} e_{2,k} + \frac{I_{pv,k} v_{pv,k}^*}{V_{pv,k}}, \\ \text{when } v_{pv,k} < V_{mpp,k} - \frac{\epsilon}{2}, \\ -\frac{e_{1,k}^2}{V_{pv,k} R_{mpp,k}} - \frac{2v_{pv,k}^* + k_{p,pv} R_{mpp,k}}{V_{pv,k} R_{mpp,k}} e_{1,k} \\ - \frac{k_{i,pv}}{V_{pv,k}} e_{2,k} - \frac{v_{pv,k}^{*2}}{V_{pv,k} R_{mpp,k}}, \\ \text{when } V_{mpp,k} - \frac{\epsilon}{2} < v_{pv,k} < V_{mpp,k} + \frac{\epsilon}{2}, \\ -\left(\frac{1}{r_{pv,k}} + \frac{k_{p,pv}}{V_{pv,k}}\right) e_{1,k} - \frac{v_{pv,k}^*}{r_{pv,k}} - \frac{k_{i,pv}}{V_{pv,k}} e_{2,k}, \\ \text{when } v_{pv,k} > V_{mpp,k} + \frac{\epsilon}{2}, \end{cases} \quad (45)$$

$$\frac{de_{2,k}}{d\tau} = C_{pv} e_{1,k}. \quad (46)$$

Linking (3) and (45), we set  $C_{pv} = 0$  to give us the algebraic solution of  $e_{1,k}$ . This is substituted into (46) to obtain the reduced-order model

$$\frac{d\bar{e}_{2,k}}{dt} = \begin{cases} \frac{k_{i,pv}}{I_{pv,k} - k_{p,pv}} \bar{e}_{2,k} - \frac{I_{pv,k} v_{pv,k}^*}{I_{pv,k} - k_{p,pv}}, \\ \text{when } v_{pv,k} < V_{mpp,k} - \frac{\epsilon}{2}, \\ -\frac{k_{i,pv}}{k_{p,pv}} \bar{e}_{2,k} - \frac{v_{pv,k}^* V_{pv,k}}{V_{pv,k} + r_{pv,k} k_{p,pv}}, \\ \text{when } v_{pv,k} > V_{mpp,k} + \frac{\epsilon}{2}. \end{cases} \quad (47)$$

Since the maximum power point is bounded by the constant voltage and constant current regions on either side, our strategy is to ensure stability on those two operating regimes, where  $|v_{pv,k} - V_{mpp,k}| > \epsilon/2$ . This approach gives stability across the entire PV curve. Following (4), the fast mode model is

$$\frac{d\tilde{e}_{1,k}}{d\tau}$$

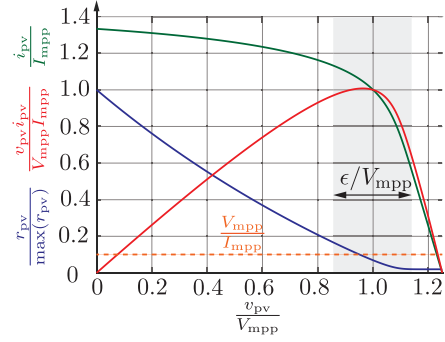


Fig. 4. Curves for PV current, power, and small-signal resistance across the operating range of voltages. Each curve is normalized to facilitate comparison. A region of width  $\epsilon$  around the maximum voltage  $V_{mpp}$  is highlighted.

$$= \begin{cases} -\frac{1}{C_{pv}} \frac{k_{p,pv} - I_{pv,k}}{V_{pv,k}} \tilde{e}_{1,k}, & \text{when } v_{pv,k} < V_{mpp,k} - \frac{\epsilon}{2}, \\ -\frac{1}{C_{pv}} \left( \frac{1}{r_{pv,k}} + \frac{k_{p,pv}}{V_{pv,k}} \right) \tilde{e}_{1,k}, & \text{when } v_{pv,k} > V_{mpp,k} + \frac{\epsilon}{2}. \end{cases} \quad (48)$$

2) *Stability and Equivalent Model:* Stability of (48) is guaranteed when  $k_{p,pv} \geq I_{pv}$ , while  $k_{i,pv} \geq 0$  gives the stability of (47). The equivalent bandwidths implied for the two regions in (47) are

$$\omega_{cc} := \frac{k_{i,pv}}{k_{p,pv} - I_{pv,k}}, \quad \omega_{cv} := \frac{k_{i,pv}}{k_{p,pv}}, \quad (49)$$

where  $\omega_{cc}$  and  $\omega_{cv}$  denote the bandwidths for the constant current and constant voltage regions characterized by  $v_{pv,k} < V_{mpp,k} - \frac{\epsilon}{2}$  and  $v_{pv,k} > V_{mpp,k} + \frac{\epsilon}{2}$ , respectively. Bandwidths for the model in (48) are

$$\omega_{cc}^f := \frac{1}{C_{pv}} \frac{k_{p,pv} - I_{pv,k}}{V_{pv,k}}, \quad \omega_{cv}^f := \frac{1}{C_{pv}} \left( \frac{1}{r_{pv,k}} + \frac{k_{p,pv}}{V_{pv,k}} \right), \quad (50)$$

where the subscripts in  $\omega_{cc}^f$  and  $\omega_{cv}^f$  conform to the notation in (49). To enforce appropriate timescale separation, we need

$$\max(\omega_{cc}^f, \omega_{cv}^f) \ll \omega_{dVOC}, \quad (51)$$

$$\max(\omega_{cc}, \omega_{cv}) \ll \min(\omega_{cc}^f, \omega_{cv}^f). \quad (52)$$

For the  $k$ -th module, plugging (49)–(50) into (51)–(52) gives the following design guidelines:

$$k_{p,pv} \geq I_{sc}, \quad (53)$$

$$\max \left( \frac{1}{C_{pv}} \frac{k_{p,pv} - I_{pv,k}}{V_{pv,k}}, \frac{1}{C_{pv}} \left( \frac{1}{r_{pv,k}} + \frac{k_{p,pv}}{V_{pv,k}} \right) \right) \ll \omega_{dVOC}, \quad (54)$$

$$\max \left( \frac{k_{i,pv}}{k_{p,pv} - I_{pv,k}}, \frac{k_{i,pv}}{k_{p,pv}} \right) \ll \min \left( \frac{1}{C_{pv}} \frac{k_{p,pv} - I_{pv,k}}{V_{pv,k}}, \frac{1}{C_{pv}} \left( \frac{1}{r_{pv,k}} + \frac{k_{p,pv}}{V_{pv,k}} \right) \right) \quad (55)$$

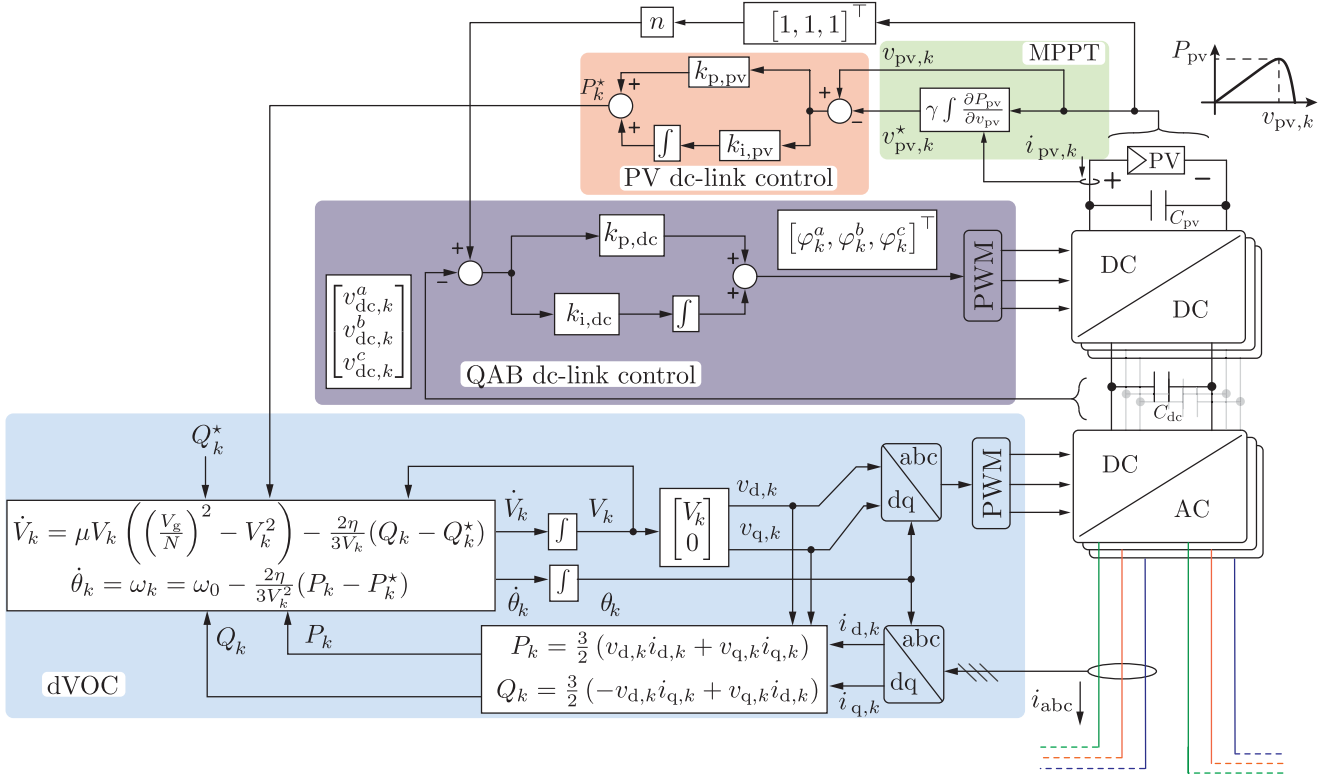


Fig. 5. The control architecture of the  $k$ -th converter module contains the following interconnected control loops: MPPT, PV dc-link control, floating dc-link controls, and dVOC-based ac-side control. The quadruple active bridge converter is compactly depicted with three dc–dc blocks, and the dc–ac H-bridge inverters interface to adjacent units in the system.

#### D. Maximum Power Point Tracking

1) *State Equations:* The MPPT controller in Fig. 5 uses  $i_{pv,k}$  and  $v_{pv,k}$  to determine the voltage reference  $v_{pv,k}^*$  for the PV dc-link regulator. Substitute the plant model in (20) into the MPPT integral control law in (21) to obtain

$$\begin{aligned} \dot{v}_{pv,k}^* &= \gamma \frac{\partial(v_{pv,k} i_{pv,k})}{\partial v_{pv,k}} = \gamma \left( v_{pv,k} \frac{\partial(i_{pv,k})}{\partial v_{pv,k}} + i_{pv,k} \right), \\ &= -2 \frac{\gamma}{R_{mpp,k}} v_{pv,k} + 2\gamma I_{mpp,k}. \end{aligned}$$

2) *Stability and Equivalent Model:* Fast inner control ensures  $v_{pv,k} = v_{pv,k}^*$  such that the MPPT law simplifies into

$$\dot{v}_{pv,k}^* = -2 \frac{\gamma}{R_{mpp,k}} v_{pv,k}^* + 2\gamma I_{mpp,k}.$$

The equivalent bandwidth of the MPPT loop becomes  $\omega_{mppt} = 2\gamma/R_{mpp,k}$  and the corresponding stability condition that enforces timescale separation is

$$\omega_{mppt} \ll \min(\omega_{cc}, \omega_{cv}).$$

The controller gain  $\gamma$  is selected such that

$$2 \frac{\gamma}{R_{mpp,k}} \ll \min \left( \frac{k_{i,pv}}{k_{p,pv} - I_{pv}}, \frac{k_{i,pv}}{k_{p,pv}} \right). \quad (56)$$

#### V. EXPERIMENTAL RESULTS

Referring to Fig. 6, we demonstrate cascaded converter operation with fully functional decentralized controls on a system

of three series-connected modules across the grid and an output filter. Module #1 was fed by a solar array simulator, whereas modules #2 and #3 were powered by a fixed dc supply. All converter modules are rated for equal power delivery and employ identical controllers with the exception that modules #2 and #3 do not have MPPT and PV dc-link controllers due to their fixed dc inputs. To carry out decentralized control, each module in Fig. 6(b) has its own control board that controls the QAB and three single-phase inverters. Each control board uses a TI-TMS280379D microcontroller. The dVOC subsystem design is constrained by:

- i) the droop conditions in (12)–(13);
- ii) ac-side stability among the  $N$  series-connected oscillator-controlled inverters [5];
- iii) stability for cascaded converters under mismatched power conditions given by (37);
- iv) stable interactions among the control loops within each module as implied in (44) and (51).

In particular, we observe that constraints (44) and (51) must hold true for varying grid strength, where  $Z_f$  takes on a range of values. Given that the dVOC controller lies at the epicenter of several potentially competing requirements, we choose its parameters (i.e.,  $\mu$  and  $\eta$ ) first among all the controllers. From there, all other control designs emanate outwardly from the dVOC subsystem such that the stability and timescale separation guidelines in (28), (51), (52), and (56) are met. Table I lists the relevant system parameters and control gains that enforce timescale separation. Fig. 7 collects the relevant bandwidths

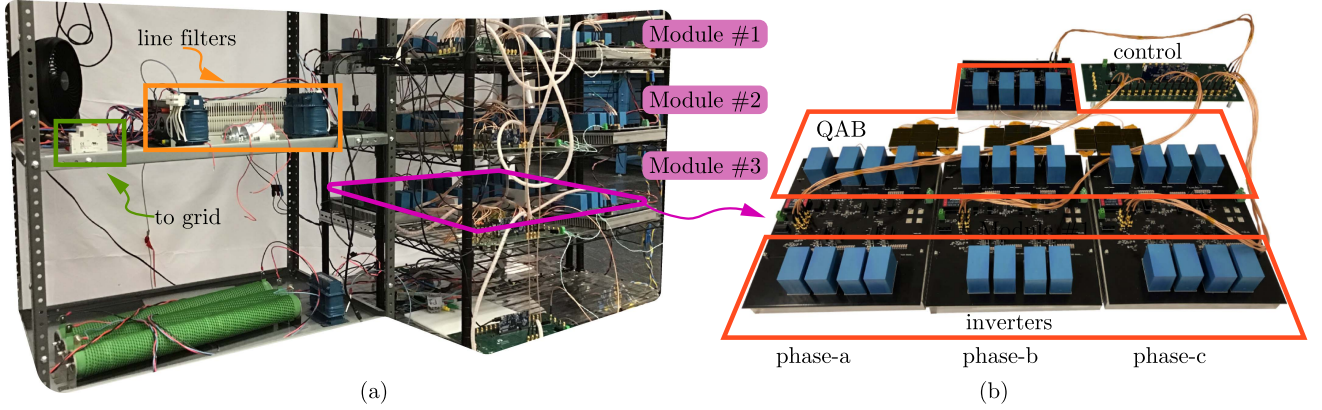


Fig. 6. The experimental setup in (a) has three converter modules with series connections on their ac sides. One converter module, as shown in (b), contains a QAB stage with high frequency magnetics along with three single-phase inverters.

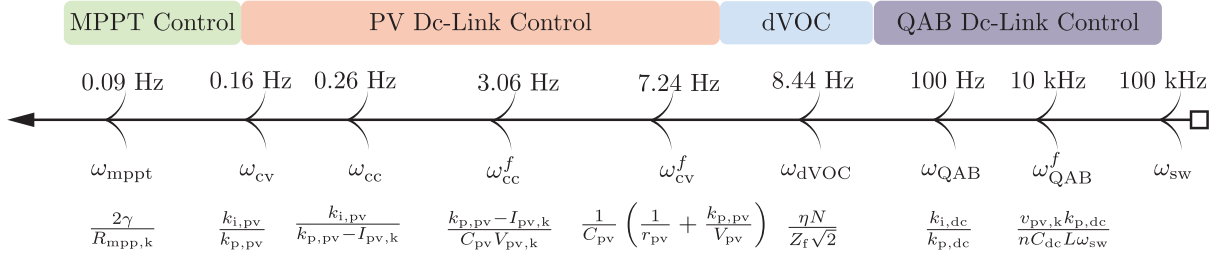


Fig. 7. Various timescale-separated controllers are shown with their respective control bandwidths that are designed through singular perturbation approach.



Fig. 8. Startup transients show three series-connected modules synchronizing to the ac grid without external communication. The modules are synchronized with zero active power transfer to the grid after 25 s. A small reactive component remains due to a mismatch between the grid voltage and sum of commanded voltages.

corresponding to each of the subsystems in the decreasing order of frequency.

#### A. Start-Up Procedure

To begin, a current-limiting resistor was added in series with the converters. Next, the inverters were effectively bypassed by turning ON the lower MOSFETs of each ac-side H-bridge. As seen on the left-hand side of Fig. 8(a), a current flows through the stack of bypassed converters that can be sensed by each module. This allows each inverter to synchronize its dVOC-based controller and begin switching with zero power commands (i.e.,  $P_k^* = 0$ ,  $k \in \{1, 2, 3\}$ ). Thereafter, the dVOC modulates each inverter and power command tracking is eventually reached such that  $P_k = 0$ ,  $k \in \{1, 2, 3\}$ . At this point, the

modules have achieved communication-free synchronization, as shown by the aligned voltage waveforms in Fig. 8(b). The modest line current that remains is purely reactive and is due to small line voltage drops and mismatches between the grid voltage and commanded values.

#### B. Nominal Operation

Power from modules #2 and #3 climb up to 200 W over 1 s after the modules have synchronized. As seen in Fig. 9(a), dc-side currents  $i_{pv,2}$  and  $i_{pv,3}$  increase to accommodate active power tracking such that  $P_k = P_k^*$ ,  $k \in \{2, 3\}$ . Module #1 power reference  $P_1^*$  originates from the upstream PV dc-link controller, which is, in turn, controlled by the MPPT control law. Power tracking in module #1 implies  $P_1 = P_1^*$ , which

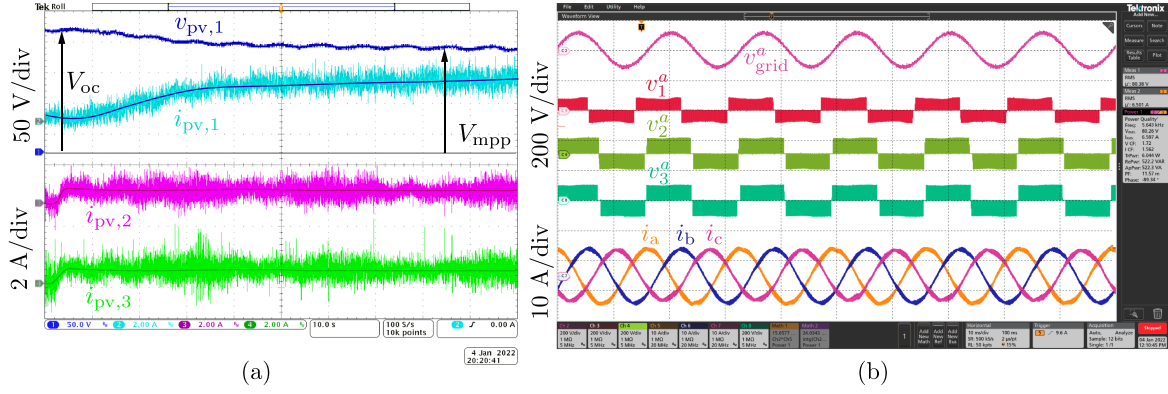


Fig. 9. Experimental results show performance of subsystems within each module for three converters connected in series across a stiff grid. MPPT integral control action for module #1 occurs across the slowest timescale where it is evident in (a) that the operating point moves from open circuit to the MPP. Modules #2 and #3 show stable operation with constant dc power. In (b), we zoom in on a few ac cycles of the phase- $a$  voltages produced by the modules and grid. Along with the regulated three-phase currents, these ac waveforms collectively show proper operation of the other controllers along with dVOC.

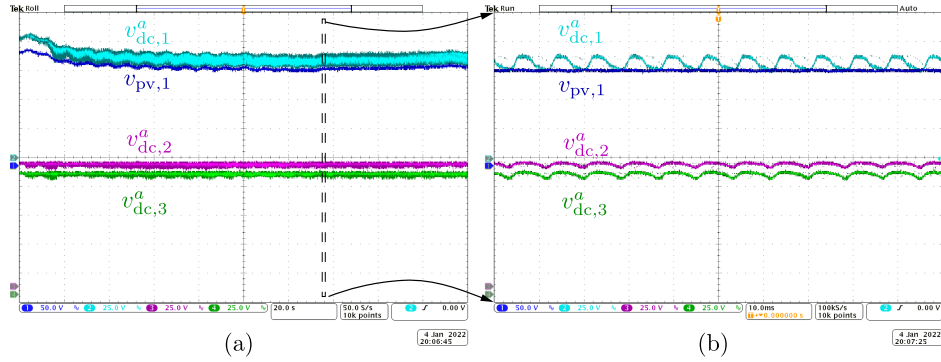


Fig. 10. Experimental results in (a) illustrate regulation of phase- $a$  QAB floating dc-link voltages in modules #1, #2, and #3. Module #1 input voltage shows a transition from the open circuit to MPP voltage. The second harmonic ripple in (b) is due to single-phase power delivery.

ensures PV dc-link voltage regulation where  $v_{pv,1} = v_{pv,1}^*$ . Thereafter, the MPPT controller continuously nudges  $v_{pv,1}^*$  until the maximum power point is reached at  $v_{pv,1} = V_{mpp}$ . While PV power ramps up, as depicted in Fig. 9(a),  $i_{pv,1}$  approaches  $I_{mpp}$  and output power becomes  $P_1 \approx P_1^* = P_{mpp}$ . Zoomed-in steady-state waveforms show a few ac cycles in Fig. 9(b). Phase  $a$  line-neutral voltages for all three modules and the grid are plotted. Switched module voltages  $v_k^a$ ,  $\forall k \in \{1, 2, 3\}$ , appropriately lead the grid waveform to ensure  $P_k = P_k^*$ ,  $k \in \{1, 2, 3\}$ .

The power reference for module #1 oscillates around its MPP of 480 W, while the reference for the other two modules are fixed at 200 W. This is reflected in the equal phase shifts of switched voltages  $v_2^a$  and  $v_3^a$  and the larger phase shift of  $v_1^a$  relative to the grid. All three modules have the same reactive power reference,  $Q_1^* = Q_2^* = Q_3^* = 0$ . However, the droop characteristic in (13) does not guarantee perfect reactive power tracking since voltage is a local quantity. Hence, the waveforms in Fig. 9(b) do imply some reactive power transfer.

To evaluate QAB dc-link voltage regulation, refer to Fig. 10(a) that shows module #1 input voltage  $v_{pv,1}$  and its trajectory from  $V_{oc}$  to  $V_{mpp}$ . Correspondingly, the phase  $a$  floating dc-link voltage  $v_{dc,1}^a$  tracks  $n v_{pv,1}$ . For the other two modules with fixed voltage inputs, the floating dc-link voltages on phase  $a$  are

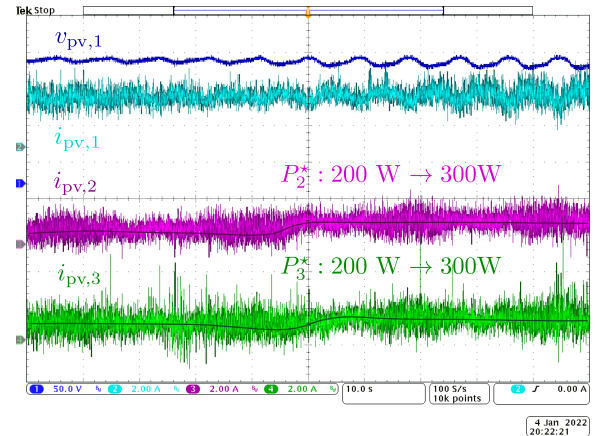


Fig. 11. Experimental results for steady operation around the MPP for module #1 during a ramp change in  $P_2^*$  and  $P_3^*$ .

held steady such that  $v_{dc,2}^a = v_{dc,3}^a$ . The floating dc-link voltages on phases  $b$  and  $c$  are identical to the phase- $a$  waveform for each respective module and are hence omitted. Inspection of the voltages in Fig. 10(b) reveals a second harmonic that is typical for single-phase power transfer. These pulsating components cancel once summed on the QAB primary input. However, the



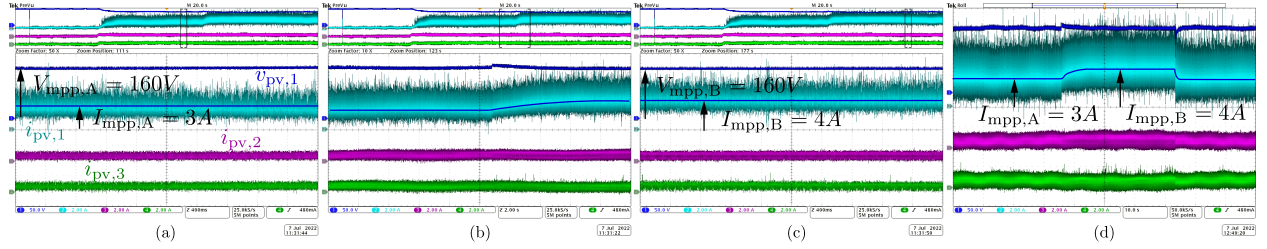


Fig. 12. Experimental results show the robustness of the cascaded set-up when PV power is suddenly changed. Steady state operation at the two PV curve-A and PV curve-B appearing in Table II is shown in (a) and (c) respectively. In (d) we show the ability of system to undergo successive transitions between the two PV curves and we zoom on one such transition in (b).

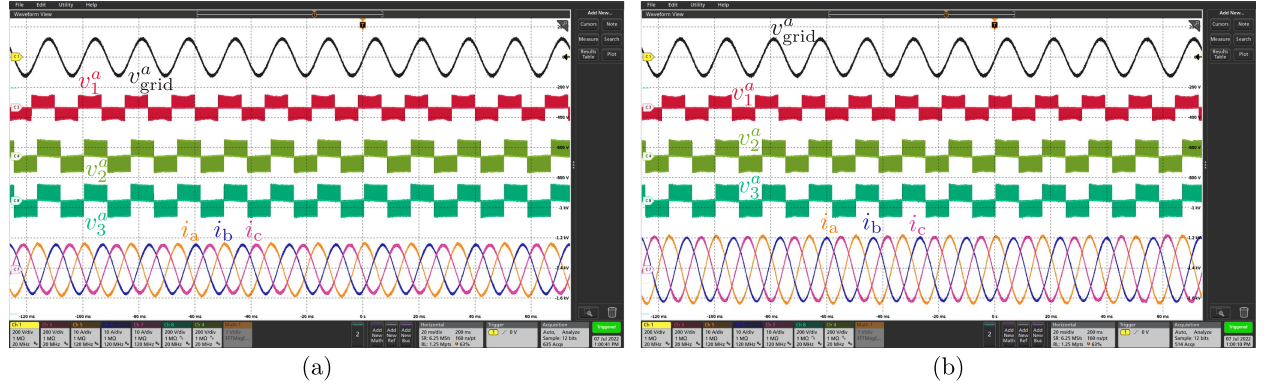


Fig. 13. AC-side waveforms for the low insolation PV curve-A and high insolation PV curve-B are shown in (a) and (b), respectively. The different power level is reflected in the ac-side currents and phase-shift between phase-*a* grid voltage and corresponding ac-side voltage of module #1.

TABLE II  
PV CURVES

Curve	$V_{mpp}$	$V_{oc}$	$I_{mpp}$	$I_{sc}$	Comments
A	160 V	200V	3 A	5 A	lower insolation
B	160 V	200V	4 A	6 A	higher insolation

switching frequency harmonics of QAB and its multiples thereof still remain in the system and can be seen in Fig. 9(a) as the background high-frequency noise in  $i_{pv,k} \forall k \in \{1, 2, 3\}$ .

### C. Response Under Dynamic Power Sharing

We now illustrate the ability of the proposed module-level control structure to preserve intended operation despite time-varying operating conditions in the remaining series-connected modules. Toward that end, we induce a 200 W  $\rightarrow$  300 W power reference step change in modules #2 and #3, and observe the response of module #1. As shown in Fig. 11, module #1 is able to maintain MPPT operation and the overall system remains stable.

We next demonstrate the stability of the cascaded system for a step change in PV power of module #1. Fig. 12(a) and (c) shows the steady-state MPP operation at the two curves described in Table II. In Fig. 12(b), we capture the transients when we suddenly switch from PV curve-A to PV curve-B, whereas Fig. 12(d) shows repeated transitions between PV curves A and B. Note that the fast transients in  $v_{pv,1}$  and  $i_{pv,1}$  are quickly damped out by the stable MPPT controller. Modules #2 and #3 continue to be regulated at  $P_k = 200$  W,  $k \in \{2, 3\}$  and are able to maintain stable operation during the PV transients

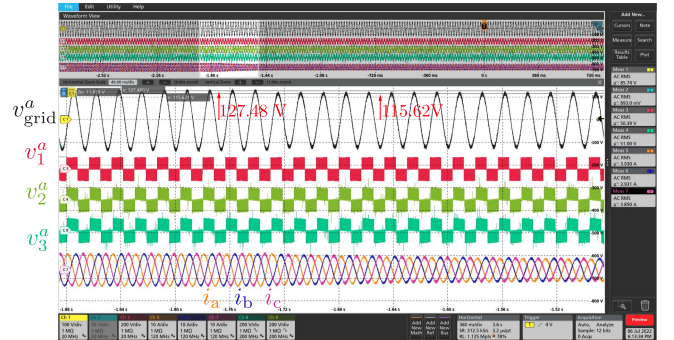


Fig. 14. Series-connected converter setup is shown to ride-through a 10% undervoltage condition. As the grid voltage reduces, the reactive power drops resulting in smaller ac-side currents.

in module #1. Fig. 13(a) and (b) illustrates the corresponding steady-state ac-side waveforms corresponding to PV curve-A and PV curve-B, respectively. Higher power operation in Fig. 13(b) is characterized by larger ac-side currents and greater phase-shift between the switched-voltage  $v_1^a$  and  $v_{grid}^a$  compared to low insolation operation in Fig. 13(a).

### D. Nonideal AC-Side Conditions

To validate grid-forming functionality, we study low-voltage and under-frequency ride-through performance of the cascaded connection. We also report the current and voltage total harmonic distortion (THD) of the two operating points given in Table II. When the grid voltage is reduced from the nominal value of 90 to 81 V in RMS, the volt-Var droop causes each module to reduce

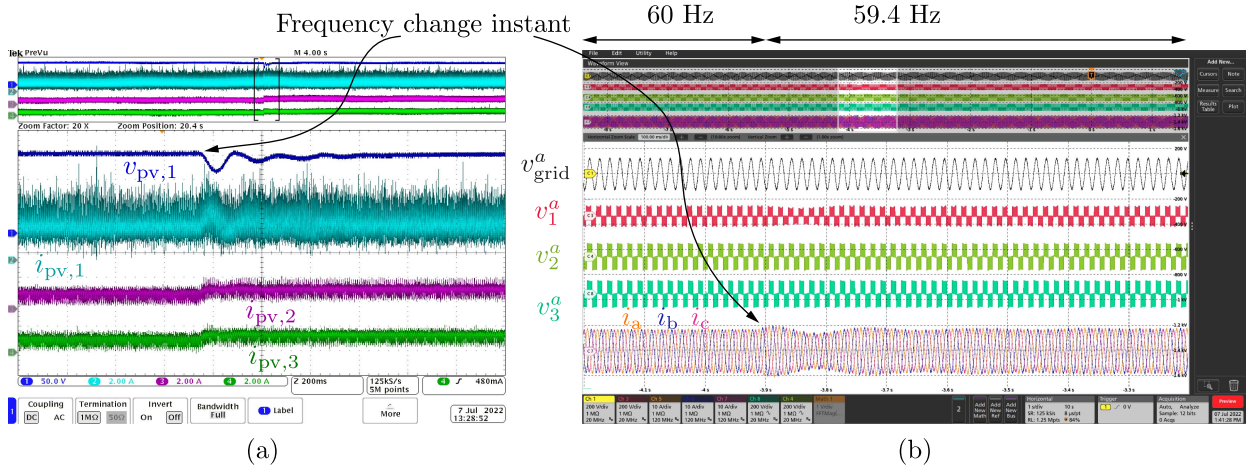


Fig. 15. Grid-forming operation is verified when the grid frequency is suddenly changed from 60 to 59.4 Hz. Module #1 connected to the PV input continues to operate at MPP. Modules #2 and #3 with constant dc-input voltage slightly increase their power output in accordance to their droop law.

TABLE III  
CURRENT HARMONICS OF AC-SIDE OUTPUT CURRENT AS PERCENTAGE

	$3 \leq h < 11$	$11 \leq h < 17$	$17 \leq h < 23$	$23 \leq h < 35$	$35 \leq h \leq 50$	TDD
IEEE 519-2014	4.0	2.0	1.5	0.6	0.3	5.0
Low Insolation (A)	0.95	0.2	0.24	0.28	0.07	1.29
High Insolation (B)	1.4	0.09	0.1	0.28	0.04	1.64

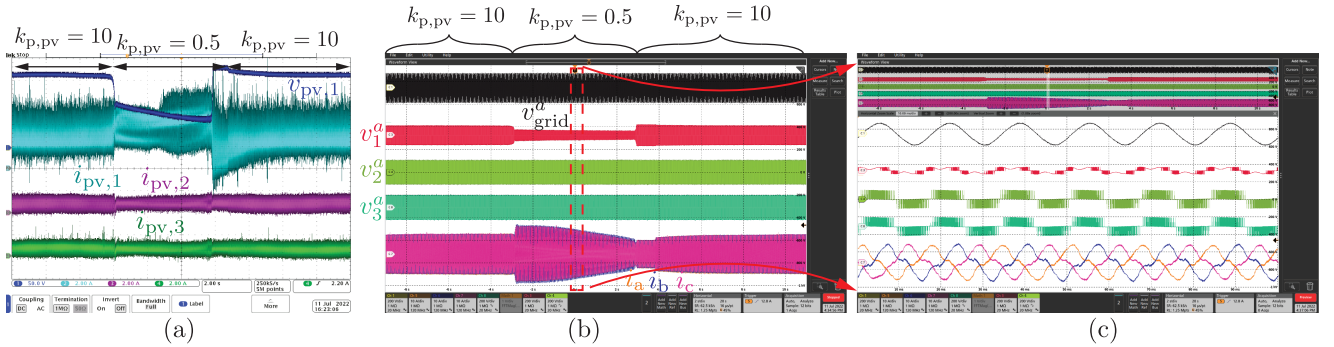


Fig. 16. Unstable dynamics between the PV dc-link controller, its adjacent dVOC, and MPPT controllers is studied, where  $k_{p,pv} = 10$  A results in a stable system and  $k_{p,pv} = 0.1$  A results in a PV voltage collapse. System stability can be restored once we revert to stable  $k_{p,pv} = 10$  A.

its reactive power output. This is reflected in the lower ac-side currents, as shown in Fig. 14.

The underfrequency response is shown in Fig. 15, where the grid-simulator suddenly changes its ac frequency from 60 to 59.4 Hz. In Fig. 15(a), modules #2 and #3 operated from a fixed voltage source can be seen to increase their dc currents. This is due to their dVOC-based ac-side control that forces an increase in active power output to restore the system frequency. However, module #1 continues to operate at the fixed MPP, and only sees a brief transient during the frequency change that is stabilized by the PV controllers. These transients are reflected in their respective ac-side waveforms shown in Fig. 15(b), where we have zoomed in on the instant of frequency change.

The voltage THD was recorded as 0.554% and 0.858% at MPP curves A and B, respectively. The current THD is calculated using specifications in IEEE standard 519-2014, as given in

Table III. A Yokogawa WT5000 power analyzer was used to record these measurements. All THD measurements are well below the recommended standards.

### E. Destabilizing Controllers

We have established the importance of the design guidelines in (28), (44), (51), (52), and (56) to obtain stabilizing controllers. We now focus on evaluating system performance when the aforementioned design rules are violated.

1) *PV DC-Link Control Instability*: The condition  $k_{p,pv} > I_{sc}$  obtained from the fast-mode dynamics of the PV dc-link controller is a new and unique contribution. We start our experiment with stable operation where  $k_{p,pv} = 10$  A. For  $I_{sc} = 4$  A, to induce instability, we switch to  $k_{p,pv} = 0.5$  A and finally revert to  $k_{p,pv} = 10$  A to demonstrate the stabilizing

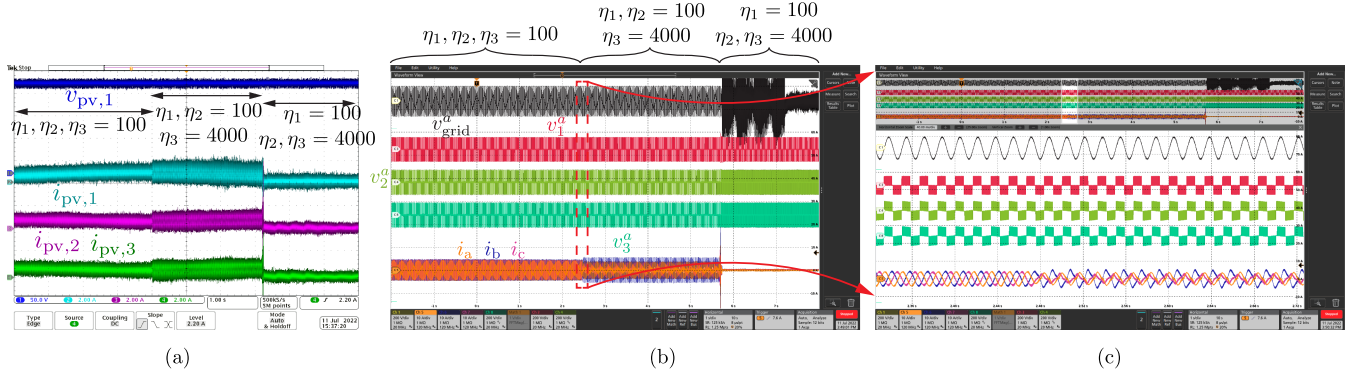


Fig. 17. Experimental results show the cascaded system performance for controllers that violate singular perturbation-based design rules resulting in unstable interaction between the dVOC and QAB dc-link controller. We change  $\eta$  from 100 (stable) to 4000 (unstable) to demonstrate the unstable interaction.

properties of the proposed controller. In Fig. 16(a) and (b), we observe the dc- and ac-side waveforms during the change in  $k_{p,pv}$ . We zoom in on a few cycles during unstable operation in Fig. 16(c), where low  $v_{pv,1}$  causes overmodulation in  $v_1^a$  and large ac-side currents.

2) *Interaction Between dVOC and QAB DC-Link:* To study the interaction between the dVOC and QAB dc-link control, we provide power for all modules with dc voltage supplies and avoid any MPPT or PV dc-link controllers. We start stable operation with  $\eta = 100$  in all three modules and then change  $\eta$  in module #3 to 4000 such that (44) is violated. This causes instability in the dc-link current, as shown in Fig. 17(a). Additionally, the ac-side currents appearing in Fig. 17(b) and shown more closely in Fig. 17(c) are highly distorted and lead to unstable operation. As we further change to  $\eta_2 = 4000$ , an extremely large overcurrent trip the cascaded converter setup.

## VI. CONCLUSION

In this article, we proposed a method to design controllers for series-connected dc-ac converters in transformerless medium-voltage applications. A hierarchy of controllers was implemented to control this converter, including MPPT, QAB floating dc voltage control, PV dc-link regulation, and ac-side power control. A singular perturbation-based controller design was implemented to decompose the system into multiple subsystems and enforce timescale separation between them. We experimentally verified the stability of the proposed approach on three 1000-W modules connected across a stiff grid.

### APPENDIX A STABILITY PROOF

The nonlinear model of the form in (2) and (3) can be used to represent any subsystem in this article. This model is linearized around its equilibrium to yield

$$\begin{aligned}\Delta \dot{x} &= A_{11}\Delta x + A_{12}\Delta z, \\ \epsilon \Delta \dot{x} &= A_{21}\Delta x + A_{22}\Delta z.\end{aligned}$$

If  $A_{22}^{-1}$  exists and if  $A_0 := A_{11} - A_{12}A_{22}^{-1}A_{21}$  and  $A_{22}$  are Hurwitz matrices, then there exists an  $\epsilon^* > 0$  such that for all

$\epsilon \in (0, \epsilon^*]$  [38, Corollary 3.1], the system (2)–(3) is asymptotically stable. The limiting value of  $\epsilon^*$  is

$$\epsilon^* = \left( \|A_{22}^{-1}\| (\|A_0\| + \|A_{12}\| \|A_{22}^{-1}A_{21}\| + 2(\|A_0\| \|A_{12}\| \|A_{22}^{-1}A_{21}\|)^{1/2}) \right)^{-1}.$$

Regarding QAB dc-link control, the dynamics in (22)–(23) imply  $A_{11} = 0$ ,  $A_{12} = C_{dc}$ ,  $A_{21} = -v_{pv,k}k_{i,dc}/nL\omega_{sw}$ , and  $A_{22} = -v_{pv,k}k_{p,dc}/nL\omega_{sw}$ . The maximum limit on  $\epsilon$  for the scalar dynamics is

$$\epsilon^* = \frac{A_{22}^2}{4\|A_{12}A_{21}\|} = \frac{v_{pv,k}k_{p,dc}^2}{4nL\omega_{sw}C_{dc}k_{i,dc}}.$$

Stability of the QAB dc-link subsystem is confirmed by ensuring  $\epsilon = C_{dc} < \epsilon^*$ .

### APPENDIX B VOLTAGE AND ANGLE DYNAMICS

The rise time of the voltage for the  $k$ -th module obtained from (14) is given by

$$t_{\text{rise}}^{V_k} = \int_{0.1V_{\text{nom}}}^{0.9V_{\text{nom}}} \frac{dt}{\mu V_k \left( \left( \frac{V_g}{N} \right)^2 - V_k^2 \right)} \approx \frac{3.0226}{\mu \left( \frac{V_g}{N} \right)^2}. \quad (57)$$

The corresponding equivalent first-order angle dynamics from (14) and (42) is

$$t_{\text{rise}}^{\delta_k} = \frac{2\ln(3)}{\omega_{\text{dVOC}}} = \frac{2\ln(3)Z_f\sqrt{2}}{\eta N}. \quad (58)$$

When analyzing the dynamics of the inverter angle  $\delta_k$ , the voltage dynamics can be ignored if  $t_{\text{rise}}^{V_k}$  is negligible compared to  $t_{\text{rise}}^{\delta_k}$ . To enforce  $t_{\text{rise}}^{V_k} \ll t_{\text{rise}}^{\delta_k}$ , from (57) and (58) we obtain

$$\frac{3.0226}{\mu \left( \frac{V_g}{N} \right)^2} \ll \frac{2\ln(3)Z_f\sqrt{2}}{\eta N} \rightarrow \frac{\eta}{\mu} \ll 1.028 \frac{V_g^2 Z_f}{N^3} =: \kappa. \quad (59)$$

For the experiment, we use  $\eta/\mu = 100/1$ , which is negligible compared to  $\kappa = 3164$  in context with the other parameters in Table I.



## REFERENCES

- [1] K. Sharifabadi, L. Harnefors, H. Nee, S. Norrga, and R. Teodorescu, *Design, Control, and Application of Modular Multilevel Converters for HVDC Transmission Systems*. Hoboken, NJ, USA: Wiley, 2016.
- [2] E. Villanueva, P. Correa, J. Rodriguez, and M. Pacas, "Control of a single-phase cascaded h-bridge multilevel inverter for grid-connected photovoltaic systems," *IEEE Trans. Ind. Electron.*, vol. 56, no. 11, pp. 4399–4406, Nov. 2009.
- [3] T. Zhao, G. Wang, S. Bhattacharya, and A. Q. Huang, "Voltage and power balance control for a cascaded H-bridge converter-based solid-state transformer," *IEEE Trans. Power Electron.*, vol. 28, no. 4, pp. 1523–1532, Apr. 2013.
- [4] X. Hou, Y. Sun, X. Zhang, G. Zhang, J. Lu, and F. Blaabjerg, "A self-synchronized decentralized control for series-connected H-bridge rectifiers," *IEEE Trans. Power Electron.*, vol. 34, no. 8, pp. 7136–7142, Aug. 2019.
- [5] S. Dutta et al., "Grid-connected self-synchronizing cascaded H-bridge inverters with autonomous power sharing," in *Proc. IEEE Energy Convers. Congr. Expo.*, 2021, pp. 2806–2813.
- [6] W. Yuan, J. Yang, G. Shi, Y. Sun, H. Han, and X. Hou, "Control design and stability analysis for the cascaded-type AC microgrid," in *Proc. 43rd Annu. Conf. IEEE Ind. Electron. Soc.*, 2017, pp. 2407–2412.
- [7] Y. Sun et al., "An  $f - P/Q$  droop control in cascaded-type microgrid," *IEEE Trans. Power Syst.*, vol. 33, no. 1, pp. 1136–1138, Jan. 2018.
- [8] J. He, Y. Li, B. Liang, and C. Wang, "Inverse power factor droop control for decentralized power sharing in series-connected-microconverters-based islanding microgrids," *IEEE Trans. Ind. Electron.*, vol. 64, no. 9, pp. 7444–7454, Sep. 2017.
- [9] J. He, Y. Liu, and Y. Wang, "Cascaded droop and inverse droop regulation for two-layer coordinated power flow control in series-connected power cells," *IEEE Trans. Ind. Electron.*, vol. 68, no. 8, pp. 6939–6951, Aug. 2021.
- [10] J. He, X. Liu, C. Mu, and C. Wang, "Hierarchical control of series-connected string converter-based islanded electrical power system," *IEEE Trans. Power Electron.*, vol. 35, no. 1, pp. 359–372, Jan. 2020.
- [11] D. Sha, G. Xu, and Y. Xu, "Utility direct interfaced charger/discharger employing unified voltage balance control for cascaded H-bridge units and decentralized control for CF-DAB modules," *IEEE Trans. Ind. Electron.*, vol. 64, no. 10, pp. 7831–7841, Oct. 2017.
- [12] S. Dutta et al., "Decentralized control of cascaded H-bridge inverters for medium-voltage grid integration," in *Proc. IEEE 21st Workshop Control Model. Power Electron.*, 2020, pp. 1–6.
- [13] L. Li et al., "Unified decentralised control for both grid-connected and islanded operation of cascaded-type microgrid," *IET Renewable Power Gener.*, vol. 14, no. 16, pp. 3138–3148, 2020.
- [14] X. Hou, Y. Sun, H. Han, Z. Liu, W. Yuan, and M. Su, "A fully decentralized control of grid-connected cascaded inverters," *IEEE Trans. Sustain. Energy*, vol. 10, no. 1, pp. 315–317, Jan. 2019.
- [15] Y. Pan, A. Sangwongwanich, Y. Yang, and F. Blaabjerg, "Distributed control of islanded series PV-battery-hybrid systems with low communication burden," *IEEE Trans. Power Electron.*, vol. 36, no. 9, pp. 10199–10213, Sep. 2021.
- [16] H. Jafarian, S. Bhowmik, and B. Parkhideh, "Hybrid current/voltage-mode control scheme for distributed AC-stacked PV inverter with low-bandwidth communication requirements," *IEEE Trans. Ind. Electron.*, vol. 65, no. 1, pp. 321–330, Jan. 2018.
- [17] X. Hou, K. Sun, X. Zhang, Y. Sun, and J. Lu, "A hybrid voltage/current control scheme with low-communication burden for grid-connected series-type inverters in decentralized manner," *IEEE Trans. Power Electron.*, vol. 37, no. 1, pp. 920–931, Jan. 2022.
- [18] B. Xu, H. Tu, Y. Du, H. Yu, H. Liang, and S. Lukic, "A distributed control architecture for cascaded H-bridge converter with integrated battery energy storage," *IEEE Trans. Ind. Appl.*, vol. 57, no. 1, pp. 845–856, Jan./Feb. 2021.
- [19] G. Shi, H. Han, Y. Sun, Z. Liu, M. Zheng, and X. Hou, "A decentralized SOC balancing method for cascaded-type energy storage systems," *IEEE Trans. Ind. Electron.*, vol. 68, no. 3, pp. 2321–2333, Mar. 2021.
- [20] L. Corradini, D. Maksimovic, P. Mattavelli, and R. Zane, *Digital Control of High-Frequency Switched-Mode Power Converters*. 1st ed., Hoboken, NJ, USA: Wiley, 2015.
- [21] M. Prodanovic and T. Green, "Control and filter design of three-phase inverters for high power quality grid connection," *IEEE Trans. Power Electron.*, vol. 18, no. 1, pp. 373–380, Jan. 2003.
- [22] M. Colombino, D. Groß, J.-S. Brouillon, and F. Dörfler, "Global phase and magnitude synchronization of coupled oscillators with application to the control of grid-forming power inverters," *IEEE Trans. Autom. Control*, vol. 64, no. 11, pp. 4496–4511, Nov. 2019.
- [23] M. Lu, R. Mallik, B. Johnson, and S. Dhole, "Dispatchable virtual-oscillator-controlled inverters with current-limiting and MPPT capabilities," in *Proc. IEEE Energy Convers. Congr. Expo.*, 2021, pp. 3316–3323.
- [24] J. M. Guerrero, J. C. Vasquez, J. Matas, L. G. de Vicuna, and M. Castilla, "Hierarchical control of droop-controlled AC and DC microgrids—A general approach toward standardization," *IEEE Trans. Ind. Electron.*, vol. 58, no. 1, pp. 158–172, Jan. 2011.
- [25] A. B. Vasil'eva and V. M. Volosov, "The work of Tikhonov and his pupils on ordinary differential equations containing a small parameter," *Russian Math. Surveys*, vol. 22, pp. 124–142, Apr. 1967.
- [26] A. B. Vasil'eva, "The development of the theory of ordinary differential equations with a small parameter multiplying the highest derivative during the period 1966–1976," *Russian Math. Surveys*, vol. 31, pp. 102–122, Apr. 1976.
- [27] H. K. Khalil, *Nonlinear Systems*, 3rd ed. Hoboken, NJ, USA: Prentice-Hall, 2002.
- [28] I. Caduff, U. Markovic, C. Roberts, G. Hug, and E. Vrettos, "Reduced-order modeling of inverter-based generation using hybrid singular perturbation," *Electric Power Syst. Res.*, vol. 190, 2021, Art. no. 106773.
- [29] S. Jafarpour, V. Purba, B. Johnson, S. Dhole, and F. Bullo, "Singular perturbation and small-signal stability for inverter networks," *IEEE Trans. Control Netw. Syst.*, vol. 9, no. 2, pp. 979–992, Jun. 2022.
- [30] Y. Chen, M. Jiménez Carrizosa, G. Damm, F. Lamnabhi-Lagarigue, M. Li, and Y. Li, "Control-induced time-scale separation for multiterminal high-voltage direct current systems using droop control," *IEEE Trans. Control Syst. Technol.*, vol. 28, no. 3, pp. 967–983, May 2020.
- [31] I. Subotić, D. Groß, M. Colombino, and F. Dörfler, "A Lyapunov framework for nested dynamical systems on multiple time scales with application to converter-based power systems," *IEEE Trans. Autom. Control*, vol. 66, no. 12, pp. 5909–5924, Dec. 2021.
- [32] J. Chow, J. Winkelman, M. Pai, and P. Sauer, "Singular perturbation analysis of large-scale power systems," *Int. J. Elect. Power Energy Syst.*, vol. 12, no. 2, pp. 117–126, 1990.
- [33] S. Zhai and S. Y. Xiao, "Bounded synchronisation of singularly perturbed complex network with an application to power systems," *IET Control Theory Appl.*, vol. 8, no. 5, pp. 61–66, 2014.
- [34] J. W. Kimball and P. T. Krein, "Singular perturbation theory for DC–DC converters and application to PFC converters," *IEEE Trans. Power Electron.*, vol. 23, no. 6, pp. 2970–2981, Nov. 2008.
- [35] Z. Yang, J. Yu, J. Kurths, and M. Zhan, "Nonlinear modeling of multi-converter systems within DC-link timescale," *IEEE Trans. Emerg. Sel. Topics Circuits Syst.*, vol. 11, no. 1, pp. 5–16, Mar. 2021.
- [36] A. Nayak, M. M. Rayguru, S. Mishra, and M. J. Hossain, "A quantitative approach for convergence analysis of a singularly perturbed inverter-based microgrid," *IEEE Trans. Energy Convers.*, vol. 36, no. 4, pp. 3016–3030, Dec. 2021.
- [37] P. K. Achanta, B. B. Johnson, G.-S. Seo, and D. Maksimovic, "A multilevel DC to three-phase AC architecture for photovoltaic power plants," *IEEE Trans. Energy Convers.*, vol. 34, no. 1, pp. 181–190, Feb. 2019.
- [38] P. Kokotovic, H. K. Khalil, and J. O'Reilly, *Singular Perturbation Methods in Control: Analysis and Design*. Philadelphia, PA, USA: SIAM, 1987.
- [39] M. Chandorkar, D. Divan, and R. Adapa, "Control of parallel connected inverters in standalone AC supply systems," *IEEE Trans. Ind. Appl.*, vol. 29, no. 1, pp. 136–143, Jan./Feb. 1993.
- [40] Q.-C. Zhong, P.-L. Nguyen, Z. Ma, and W. Sheng, "Self-synchronized synchronverters: Inverters without a dedicated synchronization unit," *IEEE Trans. Power Electron.*, vol. 29, no. 2, pp. 617–630, Feb. 2014.
- [41] B. Majmunović et al., "1 kV, 10 kW SiC-based quadruple active bridge DCX stage in a DC to three-phase AC module for medium-voltage grid integration," *IEEE Trans. Power Electron.*, vol. 37, no. 12, pp. 14631–14646, Dec. 2022.
- [42] Y. Li, J. Li, H. Xiao, J. Zhang, and Z. Du, "Stability analysis of droop-based converter using SISO method from DC side perturbation," *IEEE Trans. Power Del.*, vol. 36, no. 5, pp. 3150–3161, Oct. 2021.
- [43] S. Inoue and H. Akagi, "A bidirectional isolated DC–DC converter as a core circuit of the next-generation medium-voltage power conversion system," *IEEE Trans. Power Electron.*, vol. 22, no. 2, pp. 535–542, Mar. 2007.
- [44] M. Lu, S. Dutta, V. Purba, S. Dhole, and B. Johnson, "A grid-compatible virtual oscillator controller: Analysis and design," in *Proc. Energy Convers. Congr. Expo.*, 2019, pp. 2643–2649.



- [45] M. G. Villalva, J. R. Gazoli, and E. R. Filho, "Comprehensive approach to modeling and simulation of photovoltaic arrays," *IEEE Trans. Power Electron.*, vol. 24, no. 5, pp. 1198–1208, May 2009.
- [46] L. Niousiainen et al., "Photovoltaic generator as an input source for power electronic converters," *IEEE Trans. Power Electron.*, vol. 28, no. 6, pp. 3028–3038, Jun. 2013.
- [47] S. Maity and P. K. Sahu, "Modeling and analysis of a fast and robust module-integrated analog photovoltaic MPPT tracker," *IEEE Trans. Power Electron.*, vol. 31, no. 1, pp. 280–291, Jan. 2016.
- [48] K. Chen, S. Tian, Y. Cheng, and L. Bai, "An improved MPPT controller for photovoltaic system under partial shading condition," *IEEE Trans. Sustain. Energy*, vol. 5, no. 3, pp. 978–985, Jul. 2014.
- [49] D. S. Pillai, J. P. Ram, A. M. Y. M. Ghias, M. A. Mahmud, and N. Rajasekar, "An accurate, shade detection-based hybrid maximum power point tracking approach for PV systems," *IEEE Trans. Power Electron.*, vol. 35, no. 6, pp. 6594–6608, Jun. 2020.
- [50] R. Horn and C. Johnson, *Matrix Analysis*. Cambridge, U.K.: Cambridge Univ. Press, 2016.



**Rahul Mallik** (Student Member, IEEE) received the B.E. degree from Jadavpur University, Kolkata, India, in 2015, and the M.E. degree from the Indian Institute of Science, Bengaluru, India, in 2017, both in electrical engineering. He is currently working toward the Ph.D. degree with the University of Texas at Austin, Austin, TX, USA.

He was an Associate Scientist with Hitachi ABB Power Grids during 2017–2018 and interned at Enphase Energy, TX, USA, in 2021. Previously, he was with the University of Washington, Seattle, where

he started his Ph.D. degree in 2018. His research interests include the design, optimization, modeling, and control of high-power, high-frequency dc–dc converters, nonlinear control of grid-forming inverters, and electromechanical systems.



**Branko Majmunović** (Member, IEEE) received the B.S. degree in electrical engineering from the University of Belgrade, Belgrade, Serbia, in 2016, the M.S. degree in power electronics and drives from Aalborg University, Aalborg, Denmark, in 2018, and the Ph.D. degree from the University of Colorado, Boulder, CO, USA, in 2022.

He is currently a System Engineer with Kilby Labs, Texas Instruments, Dallas, TX, USA. His research interests include soft switching power converter design, active-bridge-based modular power converters,

high power-density converter design using widebandgap semiconductors, high-frequency magnetics design, and digital control of switched-mode power converters.



**Soham Dutta** (Student Member, IEEE) received the B.E. degree in electrical engineering from Jadavpur University, Kolkata, India, in 2015, and the M.E. degree in electrical engineering from the Indian Institute of Science, Bangalore, India, in 2017. He is currently working toward the Ph.D. degree in electrical engineering with the University of Texas at Austin, Austin, TX, USA.

His current research interests include design, modeling, and control of isolated, bidirectional cascaded dc–ac converters for medium voltage-level ultrafast

electric vehicle chargers, decentralized control of multiconverter systems, and grid-forming converters.



**Gab-Su Seo** (Senior Member, IEEE) received the Ph.D. degree in electrical engineering from Seoul National University, Seoul, South Korea, in 2015.

From 2016 to 2017, he was a Research Associate with the Colorado Power Electronics Center, University of Colorado, Boulder, CO, USA. Since 2018, he has been with the Power Systems Engineering Center, National Renewable Energy Laboratory, Golden, CO, USA, where he is currently a Senior Electrical Engineer and leads research projects focused on power electronics and power systems applications for electric grids with high penetrations of inverter-based resources. He has coauthored more than 70 IEEE journal and conference papers with one best paper award. He coauthored the *Research Roadmap on Grid-Forming Inverters* in 2020. His current research interests include power electronics for renewable energy systems and microgrids and power systems engineering for grid modernization, including grid-forming inverter control and inverter-driven power system black start for low- or zero-inertia grids to improve grid resilience and stability.

Dr. Seo is an IEEE Roadmap Working Group Chair of the International Technology Roadmap of Power Electronics for Distributed Energy Resources–WG3 Integration and Control of DER. He is an Associate Editor for the IEEE TRANSACTIONS ON POWER ELECTRONICS, *IEEE Access*, *IEEE Open Journal of Power Electronics*, and the *Journal of Power Electronics*.

Dr. Seo is an IEEE Roadmap Working Group Chair of the International Technology Roadmap of Power Electronics for Distributed Energy Resources–WG3 Integration and Control of DER. He is an Associate Editor for the IEEE TRANSACTIONS ON POWER ELECTRONICS, *IEEE Access*, *IEEE Open Journal of Power Electronics*, and the *Journal of Power Electronics*.



**Dragan Maksimović** (Fellow, IEEE) received the B.S. and M.S. degrees in electrical engineering from the University of Belgrade, Belgrade, Serbia, in 1984 and 1986, respectively, and the Ph.D. degree from the California Institute of Technology, Pasadena, CA, USA, in 1989.

From 1989 to 1992, he was with the University of Belgrade. Since 1992, he has been with the Department of Electrical, Computer and Energy Engineering, University of Colorado, Boulder, CO, USA, where he is currently a Professor and Codirector of

the Colorado Power Electronics Center. He has coauthored more than 300 publications and the textbooks *Fundamentals of Power Electronics* and *Digital Control of High-Frequency Switched-Mode Power Converters*. His current research interests include power electronics for renewable energy sources and energy efficiency, high-frequency power conversion using widebandgap semiconductors, and digital control of switched-mode power converters.

Prof. Maksimović was a recipient of the 1997 National Science Foundation CAREER Award, the IEEE Power Electronics Society (IEEE PELS) Transactions Prize Paper Award in 1997, the IEEE PELS Prize Letter Awards in 2009 and 2010, the University of Colorado Inventor of the Year Award in 2006, the IEEE PELS Modeling and Control Technical Achievement Award for 2012, the Holland Excellence in Teaching Awards in 2004, 2011, and 2018, the Charles Hutchinson Memorial Teaching Award for 2012, the 2013 Boulder Faculty Assembly Excellence in Teaching Award, the 2020 College of Engineering and Applied Sciences Research Award, the 2022 IEEE PELS R. David Middlebrook Achievement Award, and the 2023 IEEE William E. Newell Power Electronics Award.



**Brian Johnson** (Member, IEEE) received the M.S. and Ph.D. degrees in electrical and computer engineering from the University of Illinois at Urbana-Champaign, Urbana, IL, USA, in 2010 and 2013, respectively.

He is currently an Assistant Professor with the Department of Electrical and Computer Engineering, The University of Texas at Austin, Austin, TX, USA. Previously, he was with the Department of Electrical and Computer Engineering with the University of Washington in Seattle and also spent several of his

earlier years with the National Renewable Energy Laboratory in Colorado. His work was recognized with a National Science Foundation (NSF) CAREER Award in 2022. He is currently coleading the multi-institutional Universal Interoperability for Grid-Forming Inverters Consortium, which is funded by the U.S. Department of Energy. His research interests include renewable energy systems, power electronics, and control systems.